Turbulent structures of non-Newtonian solutions containing rigid polymers

M. Mohammadtabar[1], R.S. Sanders[2], and S. Ghaemi[1,a)]

[1]*Department of Mechanical Engineering, University of Alberta, Edmonton, T6G 1H9, Canada*

[2]*Department of Chemical and Materials Engineering, University of Alberta, Edmonton, T6G 1H9, Canada*

The turbulent structure of a channel flow of Xanthan Gum (XG) polymer solution is experimentally investigated and compared with water flow at a Reynolds number of Re = 7,200 (based on channel height and properties of water) and Re_τ = 220 (based on channel height and friction velocity, $u_{\tau 0}$). The polymer concentration is varied from 75, 100, and 125 ppm to reach the point of maximum drag reduction (MDR). Measurements are carried out using high-resolution, two-component PIV to capture inner and outer layer turbulence. The measurements showed that the logarithmic layer shifts away from the wall with increasing polymer concentration. The slopes of the mean velocity profile for flows containing 100 and 125 ppm XG are greater than that measured for XG at 75 ppm, which is parallel with the slope obtained for deionized water. The increase in slope results in thickening buffer layer. At MDR, the streamwise Reynolds stresses are as large as those of the Newtonian flow while the wall-normal Reynolds stresses and Reynolds shear stresses are significantly attenuated. The sweep-dominated region in the immediate vicinity of the wall extends further from the wall with increasing polymer concentration. The near-wall skewness intensifies towards positive streamwise fluctuations and covers a larger wall-normal length at larger DR values. The quadrant analysis at y^+_0=25 shows that the addition of polymers inclines the principal axis of v versus u plot to almost zero (horizontal) as the joint probability density function (JPDF) of fluctuations becomes symmetric with respect to u axis at MDR. The reduction of turbulence production is mainly associated with attenuation of the ejection motions. The spatial-correlation of the fluctuating velocity field shows that increasing polymer concentration increases the spatial coherence of u fluctuations in the streamwise direction while they appear to have opposite sign in the wall-normal direction. The proper orthogonal

[a] Author to whom correspondence should be addressed. Email: ghaemi@ualberta.ca

decomposition (POD) of velocity fluctuations shows that the inclined shear layer structure of Newtonian wall flows becomes horizontal at the MDR and does not contribute to turbulence production.

I. Introduction

There are several additives for drag reduction in liquid flows such as fibers, surfactants, micro-bubbles, and polymers. The latter has been the most common technique in oil pipelines industry because small quantities of polymer molecules can significantly reduce drag.[1] For example, Luchik et al.[2] demonstrated that polymer concentrations as small as 1-3 ppm can reduce drag by 20-30% and an even greater drag reduction effect (69%) was observed by Warholic et al.[3] at 50 ppm. Several polymers with different structures have been investigated to evaluate drag reduction (DR) performance and provide insight into the DR mechanisms.[4] Most of these polymers are synthetic such as polyethylene (PEO), polyacrylamide (PAM) and polyisobutylene (PIB) and have been successfully tested in both pilot-scale and industrial applications.[4,5] It is currently of interest to replace these additives with biopolymers, such as Guar Gum, Xanthan Gum (XG), Okra, Aloe Vera, and Glycogen. Biopolymers are generated from living organisms and are bio degradable, i.e. they break down into natural products such as water, gases, and salts. Therefore the use of biopolymers results in the reduction of the environmental footprint associated with the producing, consuming and disposal of drag-reducing polymers[5].

Polymers are generally classified as flexible or rigid polymers, based on their molecular structure. Flexible polymers are more effective in reduction of skin-friction than rigid polymers[6-10] but are more susceptible to mechanical degradation due to shear flow than rigid polymers.[10] Most biopolymers such as Guar Gum, XG, sodium alginate, glycogen, and starch are categorized as rigid polymers. Among these, XG has a wide range of applications in the food production, cosmetics, pharmaceutical and oil industries. The XG polymer is an extracellular polysaccharide which is made by the bacterium Xanthomonas camperstris.[11] It shows a stable organized helical conformation which is the reason for its rigid structure at moderate temperature and low ionic forces.[10] Under saline conditions, or at high temperatures, its configuration changes to a coiled structure which is associated with poorer drag reduction performance.[10] The drag reduction obtained by XG, similar to the performance observed when flexible polymers are used, increases

as its concentration and molecular weight increases.[12,13] However, the transient performance (DR versus time) for flexible and rigid polymers has been observed to be significantly different.[10]

There are currently two DR mechanisms describing the interaction of the polymer molecules with turbulent motions. Lumley[14] described the DR based on extension of polymers and increase of the effective (extensional) viscosity of the solution. Increasing effective viscosity results in damping of small eddies, increasing the buffer layer thickness, and consequently producing DR. The second scenario presented by Gennes[15] focuses on elastic effects of polymers. Turbulent velocity fluctuations at small scales are reduced because of the elasticity of the polymers. This theory assumes that the turbulent energy is stored as elastic energy by the polymer molecules and is released far away from the wall somewhere in the buffer layer or log layer.[16,17] However, the applicability of the second DR mechanism based on elasticity of the polymers for rigid polymers such as XG needs to be further explored.[10,18] Virk et al.[19] also describes two different drag reduction behaviors based on friction factor versus Reynolds number experiments for flexible, random-coiling, deformable additives (introduced as Type A), and relatively rigid, elongated, undeformable additives (Type B). Therefore, for better understanding of DR using biopolymers (such as XG), investigation of the interaction of rigid polymers with turbulent structures is required.

The effect of flexible polymers on turbulence structures has received more attention in the literature due to their superior DR performance. Warholic et al.[3] carried out laser Doppler velocimetry (LDV) measurements of polymeric solutions containing a flexible polymer (Percol 727, a copolymer of PAM and sodium acrylamide) in the DR range of 10-69% at $Re \sim 20{,}000$. They observed an increase of the intercept value (B) of the log-law of the mean velocity profile for DR < 40% while the slope of the log-law ($1/\kappa$) increases at DR > 40%. The streamwise Reynolds stress normalized with friction velocity of the associated polymer solution ($\langle u^2 \rangle / u_\tau^2$) increased with the increasing DR for DR ≤ 40% while it decreased for DR > 40%. However, normalized wall-normal Reynolds stress ($\langle v^2 \rangle / u_\tau^2$) and the Reynolds shear stress ($\langle uv \rangle / u_\tau^2$) decreased with increasing DR until the point of maximum drag reduction (MDR) was reached. The latter results confirmed the existence of a "shear deficit", which shows that the total shear stress in drag reducing flow is greater than the sum of viscous shear stress and the Reynolds shear stress. The shear deficit is equivalent to polymeric stresses. Ptasinski et al.[20] also carried out LDV

measurements on the turbulent pipe flow of a flexible PAM polymer (Superfloc A110). They observed a similar trend in variations of turbulence statistics with increasing DR although a larger $\langle uv \rangle$ residual (maximum of 0.014 N/m^2 at 69% DR) was observed at MDR compared to the findings of Warholic et al.[3] (maximum of 0.005 N/m^2 at 65% DR).

The effect of molecular weight,[11] polymer concentration,[13] solution temperature,[13] and salt (NaCl)[12] concentration on the rheological and turbulent DR performance of rigid XG polymers has been investigated and reported previously in the literature. Generally, the results show that DR of XG solutions increases with increasing polymer concentration and molecular weight while DR performance decreases at higher temperatures. The Reynolds stresses in turbulent flows of rigid XG polymers were investigated by Escudier et al.[7] and Jaafar and Poole[9]. The LDV measurements of Escudier et al.[7] demonstrated that the spanwise Reynolds stress ($\langle w^2 \rangle / u^2_\tau$) is independent of the extent of DR, but $\langle v^2 \rangle / u^2_\tau$ decreases with increasing DR, and $\langle u^2 \rangle / u^2_\tau$ increases as DR increases when DR $\leq$ 59%. Any further increase in DR is associated with smaller values of $\langle u^2 \rangle / u^2_\tau$. As mentioned above, the Reynolds stresses were normalized with the friction velocity of the polymer solution; therefore, the trends are also affected by the variation of friction velocity with DR.

The objective of the current investigation is to characterize the turbulent structure of a representative rigid biopolymer, XG, at a relatively low Reynolds number (Re = 7,200), and to quantify differences in the turbulent structures at a range of polymer concentrations up to (and including) the concentration providing MDR. High spatial-resolution PIV is conducted to investigate the DR mechanism by studying (and comparing) the turbulent structure of water and polymer solutions. In this study, and in contrast with most of the results presented in the literature, the Reynolds stresses are normalized using a common friction velocity ($u_{\tau 0}$ of Newtonian flow) to more clearly identify the physical variations in the turbulent flows. The investigation is extended to higher-order moment of velocity fluctuation and conditional average of Reynolds shear stress to identify the relationship between reduction of turbulence production and turbulent coherent structures. In addition, the length-scales and spatial organization of turbulent motions are characterized using spatial-correlation and Proper Orthogonal Decomposition (POD).

II EXPERIMENTAL SETUP

Characterization of the turbulent structure is carried out using planar PIV measurement in a turbulent channel flow of water (Newtonian) and XG polymeric solutions (non-Newtonian). Experiments are carried out at 21.9 L/min of XG solutions at polymer concentrations of 75, 100, and 125 ppm concentration in deionized water. For brevity, the XG concentrations of 75 ppm, 100 ppm, and 125 ppm are indicated as XG-75, XG-100, XG-125, respectively. The flow facility, pressure drop measurement, polymer preparation procedure, and the PIV system are described in this section.

A. Flow loop

The measurements are carried out in the test-section of a closed-circuit flow loop with rectangular cross-section of 60×10 mm^2 (W×H) and hydraulic diameter of D_h = 17.1 mm. The top and bottom plates of the test section are made from cast acrylic while the sidewalls are glass to minimize distortion of high-magnification PIV images. The total length of the rectangular channel is 1200 mm (120H) while the measurements are carried out 845 mm (84.5H) downstream of the channel entrance to obtain a fully developed channel flow. There is a settling chamber upstream of the test-section followed by a contraction section with area ratio of 1:9 and a diffuser downstream of the test section as shown in Figure 1. The upstream settling chamber has a honeycomb structure to break down the large eddies and a fine mesh to increase the uniformity of the flow at the entrance of the test-section.

The flow loop has a 70 L reservoir connected to a Moyno pump (Model 36704). The relatively large liquid volume along with the low shear-rates within this type of pump reduces the degradation rate of polymer solution. Previous investigations have shown rapid degradation of polymers when centrifugal or gear pumps are used.[21] A variable frequency driver (VFD) is used to control the pump speed while a magnetic flow meter (Omega, FLR 8340D) measures the flow rate. Flow rate data were collected at a frequency of 2 Hz. A constant Reynolds number of Re = 7,200 was chosen for these experiments, where Re is defined as $Re = U_bH/\upsilon$, and U_b, H, and υ are the bulk velocity, channel height, and dynamic viscosity of water, respectively. The bulk velocity is kept at 0.61 m/s. The inner scaling of the turbulent Newtonian channel flow (water) can be estimated using Blasius' law estimating the friction-factor as $C_f = 0.0791(U_bD_h/\upsilon)^{-1/4} \sim 0.0075$.[22,23] The estimated C_f is applied to calculate the wall shear stress as $\tau_{w0} = 0.5\rho U_b^2 C_f \sim 1.53$ Pa and the

friction velocity is therefore $u_{\tau 0} = (\tau_{w0}/\rho)^{0.5} \sim 0.039$ m/s. The estimated wall unit is $\lambda_0 = \upsilon/u_{\tau 0} = 22.8$ μm and $Re_\tau = u_{\tau 0}H/(2\upsilon) = 220$.[23]

A Validyne differential pressure transducer with 0.5 psi diaphragm is used to measure the pressure drop between pressure Ports 1 and 2, as shown in Figure 1. The high-pressure port is located at $x = 0.3$ m from the entrance of test section (the coordinate system is shown in Figure 1) to ensure fully developed flow,[24] and the low-pressure port is installed at $x = 1$ m. The pressure transducer is calibrated using pressure calibrator DPI 610. The voltage output for both pressure drop measurement and flow rate is read using a data acquisition card (National Instruments 9219) with 24-bit resolution and logged using LabVIEW. The data collection frequency for pressure drop measurement was 2 Hz.

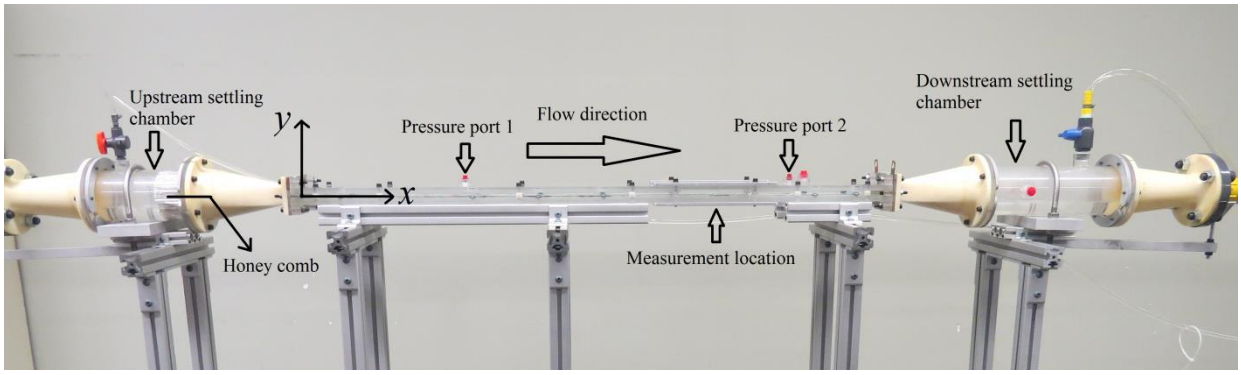

FIG. 1. The test-section of the present study, which has a rectangular cross-section formed by glass side walls and acrylic top and bottom walls.

B. Polymer solution

The applied XG is a biopolymer made from the process of fermentation of Xanthomonas by gram-negative bacteria.[25] The XG polymer has a linear main-chain of (1-4)-β-D glucose backbone, connected to a trisaccharide side-chain on every second D-glucose. The rigidity of the polymer is produced by the charged trisaccharide side-chain which folds back around main chain of (1-4)-β-D glucose.[12] Based on the literature, the molecular weight of XG polymer is between 2×10^6 and 5×10^7 g/mol.[25]

A high-concentration, master XG solution is prepared using a low shear magnetic stirrer. The required amount of XG polymer is accurately weighed (Mettler Toledo, AB104-S) with precision of 0.1 mg. The polymer and water were gradually added to a beaker (~2 L) while the magnetic

stirrer mixed the solution at 300-400 rpm. This procedure prevents aggregation of polymer molecules and lump formation. The length of the magnetic stir bar was 60-70% of the beaker diameter to promote homogenous mixing. After 2 hours of mixing, a vacuum pump was applied to remove air bubbles from the solution. The master solution was added to ~ 68 L of water to obtain the desired final concentration (75, 100, 125 ppm) in the flow loop.

The wall shear stress of polymer solutions is estimated using pressure drop measurement as $\tau_w^* = \Delta P\ WH\ /\ 2L(W+H)$, where ΔP and L are pressure drop and distance between two pressure ports, respectively.[3] As mentioned previously, the experiments of the current study are carried out at a constant flow rate and the percentage of drag reduction (DR) achieved for each polymer solution is obtained using

$$DR\% = \left(1 - \frac{\Delta P_{polymer}}{\Delta P_{water}}\right) \times 100 \quad (1)$$

The wall shear stress can also be obtained using $\tau_w = \mu_w d\langle U\rangle/dy$, where μ_w and $d\langle U\rangle/dy$ are dynamic viscosity and shear rate of polymer solution at the wall, respectively.[8,20] Here, the shear rate at the wall is estimated using high-spatial resolution PIV measurement (detailed in the next section); specifically, by producing a best-fit linear regression of the near-wall velocity points. The estimated shear rate is used to obtain the corresponding near-wall viscosity (μ_w) from viscosity measurement presented in Figure 2. Finally, wall shear stress is calculated by multiplying viscosity (μ_w) and shear rate ($d\langle U\rangle/dy$) at the wall. It is important to note that the application of a constant near-wall viscosity for non-Newtonian flows is an approximation.[26] The shear stress obtained from PIV is within 15% of that estimated based on pressure drop. The variation of wall-shear stress over the corners and the side walls of a finite duct introduces error in the latter method. A rheometer with a double gap cylinder (RheolabQC, Anton Paar USA Inc.) is used to measure the viscosity of each solution up to shear-rate of 1000 (1/s).[27] The estimated inner-wall scaling of the polymer and water channel flows and the relevant parameters are shown in Table 1. As Table 1 shows, drag reduction clearly increases with increasing XG concentration.

The Fanning friction factor versus Reynolds number ($Re_w = \rho U_b D_h/\mu_w$) for water and polymer solutions is shown in Figure 3. The Fanning friction factor is calculated through $C_f = 16/Re_w$ for laminar flow and $1/C_f^{1/2} = 4\log_{10}(Re_w\ C_f^{1/2}) - 0.4$ (Prandtl-Karman equation) for turbulent flow.[4,8] Virk et al.[28] showed the point of MDR using polymers reaches an asymptote which can be modeled

as $1/C_f^{1/2} = 19\log_{10}(Re_w C_f^{1/2}) - 32.4$ on the Fanning plot. The friction factor for water is in good agreement with Prandtl-Karman equation for turbulent flows. It is also observed in Figure 3 that the friction factor decreases with increasing polymer concentration. It should be noted that MDR was reached at XG-125 (i.e. a polymer concentration of 125 ppm). It can be seen in Figure 3 that the friction factor for this condition (XG-125) overlaps with the Virk's asymptote. Further evidence of the turbulent regime for polymeric flows is provided using spectral analysis in spatial domain in Figure 14 of the Appendix section.

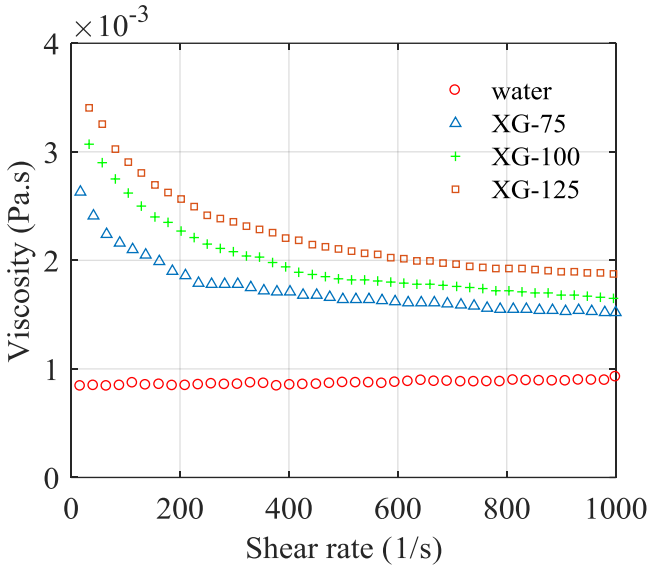

FIG. 2. Rheological characterization of water and polymer solutions showing the effect of XG polymer concentration on the solution viscosity.

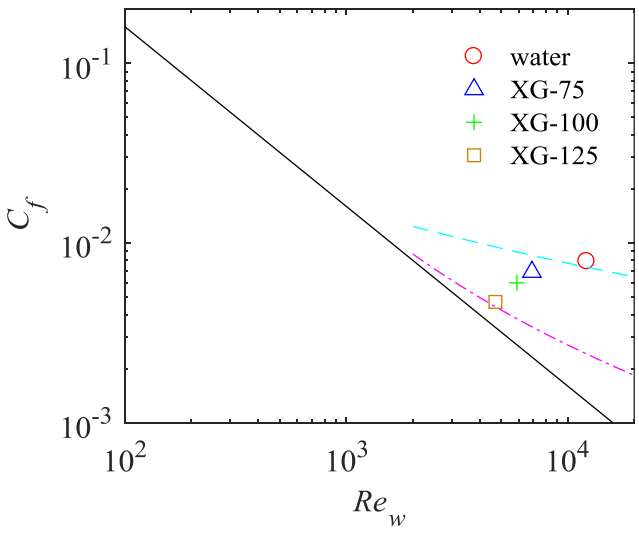

FIG. 3. The effect of XG polymer concentration on Fanning friction factors obtained from experimental measurements. Solid line shows $C_f = 16/Re_w$ (laminar flow), Prandtl-Karman equation for turbulent flows (---), Virk's asymptote (-·-·-).

Table 1. Drag reduction and channel flow scaling for water and the XG polymer solutions. DR% is calculated based on τ_w.

	C_f	DR%	τ_w (Pa)	τ_w^* (Pa)	u_τ (m/s)	μ_w (Pa.s)	λ (μm)	d<*U*>/*dy* (1/s)
water	0.0079	0	1.602	1.37	0.0400	0.89×10^{-3}	22.2	1800
XG-75	0.0069	17	1.331	1.14	0.0365	1.53×10^{-3}	42.0	870
XG-100	0.0060	36	1.037	0.89	0.0322	1.7×10^{-3}	52.9	610
XG-125	0.0047	45	0.880	0.75	0.0296	2.2×10^{-3}	74.4	400

C. Planar particle image velocimetry

Planar PIV measurement at relatively high image magnification (M = 1.3) was carried out across the full height channel. A Nd:YAG laser (Solo III-15, New Wave Research) with 532 nm wave length, and maximum output of 50 mJ over 3-4 ns pulse was applied for illumination. A combination of cylindrical and spherical lenses was used to form a laser sheet having a thickness of ~ 1 mm. The laser sheet was directed through the bottom wall of the test section to cover an *x*-*y* plane at the mid-span of the cross-section. A CCD camera (Imager proX, LaVision GmbH) with sensor size of 2048×2048 pixel and pixel size of 7.4×7.4 μm^2 with 14-bit resolution was employed to capture the scattered light reflected from 2 μm silver coated spherical glass beads. The tracers have a density of 4 g/cm^3 (SG02S40 Potters Industries) and relaxation time $\tau_s = d_p^2\rho_p/18\mu$, ~ 10^{-6} s, where d_p is the tracer particle diameter, ρ_p is tracer particle density, and μ is viscosity of water. The camera is equipped with a Sigma SLR objective lens with a focal length of f = 105 mm at an aperture opening of f/11. The current PIV measurement has the digital resolution of 179 pix/mm. Field of view of the image is 11.5×11.5 mm^2 and depth-of-field is set to approximately 1 mm. An ensemble of 6,000 PIV image pairs is recorded in double-frame mode with laser pulse separation of 110 μs synchronized using a programmable timing unit (PTU9, LaVision GmbH) controlled by DaVis 8.2.

The minimum intensity of the ensemble of images was subtracted from individual images in order to improve the signal-to-noise ratio. The resulting images were multiplied by a constant to utilize the 14-bit resolution before normalizing the images by the average of the ensemble. The ensemble

of correlation (EC) technique (Meinhart et al.[29]) with final interrogation window (IW) size of 8×8 pix (45×45 μm^2) and 75 percent overlap was applied to obtain the mean velocity profile. The high spatial-resolution of this technique allows measurement of the velocity gradient within the viscous sublayer and subsequent estimates of the wall shear rate, as was mentioned previously. The turbulence statistics are obtained from a multi-pass correlation algorithm applied to double-frame recordings with final interrogation windows of 32×32 pix (0.18×0.18 mm^2, 7.9λ_0×7.9λ_0) with 75 percent overlap. The PIV processing was conducted in DaVis 8.2 (LaVision GmbH). The smallest eddy size in wall turbulence which should be resolved to obtain accurate turbulence statistics is ~20λ_0 (~455 μm) according to Stanislas et al.[30]. This eddy size is larger than the IW size (7.9λ_0) demonstrating the adequate spatial resolution of the current PIV system. A summary of the measurement parameters can be found in Table 2.

Table 2. Imaging and processing parameters of the planar PIV system.

Data set	6,000	
Magnification	1.3	
Digital resolution	179 pix/mm	
Δt (μs)	110	
Measurement field (Δx, Δy)	2048×2048 pix 11.5×11.5 mm^2 505.5 λ_0×505.5 λ_0	
Velocity evaluation	double-frame correlation	ensemble of correlations
Spatial resolution (x, y)	32×32 pix 180×180 μm^2 7.9 λ_0×7.9 λ_0	8×8 pix 45×45 μm^2 2.0 λ_0×2.0 λ_0
Window overlap	75 %	75 %

III. RESULTS AND DISCUSSION

In this study, the turbulent structure of XG polymer solutions is investigated to identify the different mechanisms contributing to drag reduction. Additionally, the turbulent structures in the non-Newtonian polymer solutions are compared with those found in Newtonian turbulent channel flow. The mean velocity, higher order turbulence statistics, velocity fluctuations in different quadrants, and length scale of the turbulent structures are investigated. Proper Orthogonal Decomposition (POD) is also utilized to further characterize the spatial pattern of the energetic turbulent modes.

A. Mean velocity profile

The profiles of mean streamwise velocity $\langle U \rangle$ normalized by U_b across half the channel for water and the XG solutions are presented in Figure 4a. The velocity gradient ($d\langle U \rangle/dy$) at the wall reduces with increasing XG concentration. This results in the observed reduction of wall-shear stress in Table 1. The profiles also tend toward a parabolic distribution similar to a laminar channel flow. However, the flow is still in the turbulent regime as was shown earlier based on the Fanning plot of Figure 3. At a constant flow rate, an increase in polymer concentration reduces the near-wall velocity while increasing the velocity in the core of the flow.

The profiles of $U^+ = \langle U \rangle / u_\tau$, plotted against wall-normal distance $y^+ = y/\lambda$, are shown using a semi-logarithmic scale in Figure 4b. The friction velocity (u_τ) and wall unit (λ) of each polymer are presented in Table 1. The water profile follows the von-Karman log law ($U^+ = 1/\kappa \, ln \, y + B$) with $\kappa = 0.4$ and $B = 5.5$, confirming its fully developed state.[4] The U^+ profiles for the water and polymer solutions overlap within the viscous sublayer ($y^+ < 5$) while the polymer solutions continue to follow the law of the wall at larger values of y^+. A considerable dependence of U^+ on XG concentration is observed beyond the viscous sublayer ($y^+ \sim 15$). A thicker viscous sublayer and buffer layer, and an upward shift of the log-layer are observed with increasing polymer concentration. This indicates larger viscous dissipation by the smallest eddies in the near-wall region while the balance between production and viscous dissipation (i.e., log layer) occurs farther away from the wall. A log-layer is observed for XG-75 within $35 < y^+ < 120$ with fitted $\kappa = 0.4$, which is similar to the Newtonian flow. However, for XG-100, κ reduces to 0.32 while the log-layer is approximately bounded by $40 < y^+ < 90$. No distinct log-layer is observed for the maximum drag reduction case of XG-125. Virk et al [31] postulated an additional "interactive zone" which

connects the Newtonian-type viscous and turbulent zones. This is different from a Newtonian turbulent wall flow in which the viscous sublayer and the turbulent log-layer are connected only via a buffer region. The amount of drag reduction was associated with the extent of the interactive zone. Virk et al [31] also anticipated that the ultimate drag reduction is achieved when the interactive zone extends to the channel centerline, as is observed here for the XG-125 condition, as shown in Figure 4b. It should be noted XG-125 reaches the maximum drag reduction (MDR) asymptote ($u^+ = 11.7\ ln\ y^+ - 17$) proposed by Virk et al [31].

The current investigation is carried out at a constant flow rate while the addition of polymers decreases the friction velocity and increases fluid viscosity at the wall. Therefore, Re_τ reduces to 117, 93, 66 for XG-75, XG-100, and XG-125. In order to distinguish the effect of reduction in Re_τ from drag reducing effect of polymers, mean velocity profile from DNS of Newtonian flow by Tsukahara et al.[32] at $Re_\tau = 70$ is added to Figure 4b. The added mean velocity profile follows is close to the profile of XG-75 at $Re_\tau = 117$. Therefore, the effect of polymer is beyond merely reduction of Re_τ or laminarization of the flow field.

The maximum drag reduction (MDR) is valid for both flexible and rigid polymer solutions. However, these two polymer types approach MDR in the different ways with increase of concentration according to Procaccia et al.[33]. The mean velocity profile of flexible polymers follows the MDR asymptote until a crossover point where it becomes parallel to the Newtonian log-law with $\kappa = 0.4$ and $B = 5.5$ (i.e., Newtonian plug). The crossover point is further away from the wall as DR of the flexible polymer increases. On the other hand, the semi-logarithmic profile of rigid polymers prior to MDR does not follow the MDR near the wall. It falls between the Newtonian log-law and MDR profiles. The results of current study in Figure 4b and also Escudier et al.[8] confirm this trend for rigid polymers. The exception to this trend is the result of Warholic et al.[3], which shows mean velocity of a flexible polymer is between the Newtonian log-law and MDR profile before reaching MDR.

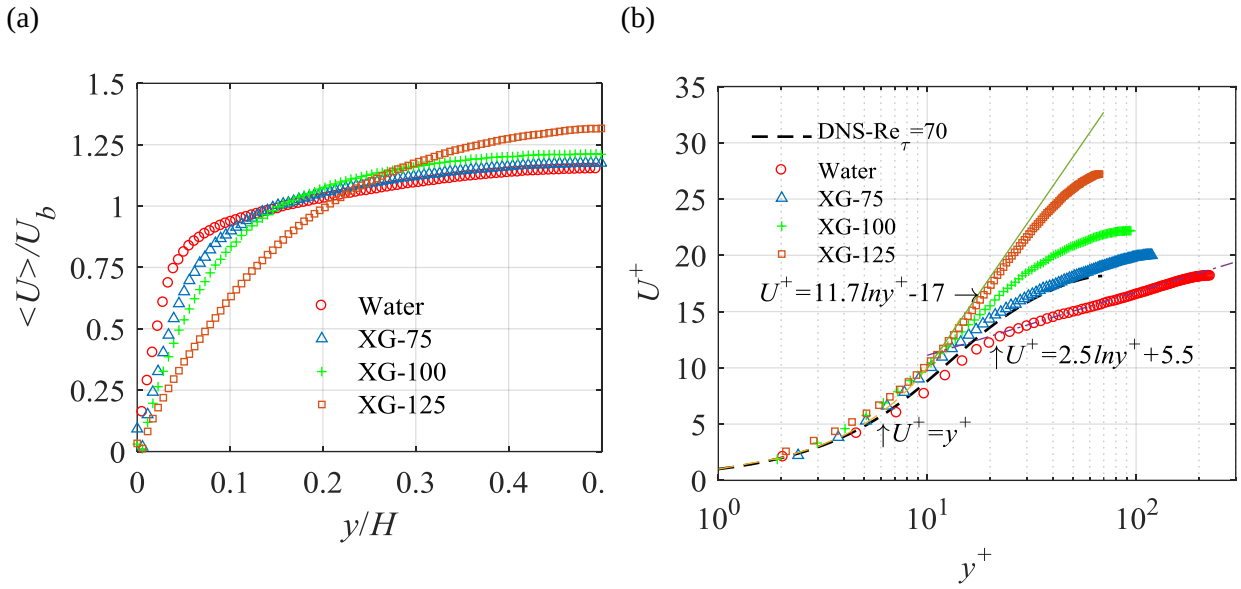

FIG. 4. The effect of XG polymer concentration on mean streamwise velocity profiles (a) normalized by the bulk velocity versus location/H across the channel, and (b) normalized by friction velocity and plotted against y^+. Only one out of five data points is presented for clarity of the plot. The law of the wall ($U^+=y^+$), log-law of Newtonian flows ($U^+=2.5\ln y^+ +5.5$), and Virk's asymptote ($U^+=11.7\ln y^+ -17$) are also indicated in this figure. Profiles of U^+ from DNS of Tsukahara et al.[32] at Re_τ = 70 in water are also shown for comparison.

B. Reynolds stresses

The dimensionless streamwise normal Reynolds stress profiles, $\langle u^2\rangle/u^2_{\tau 0}$ are shown in Figure 5(a). The measurement in Newtonian flow is also compared with the DNS results of Tsukahara et al.[32] at Re_τ=180 due to the unavailability of DNS at Re_τ = 220. The DNS data is normalized using its corresponding $u_{\tau 0}$ at Re_τ=180. There is an overlap between the DNS and PIV measurement in water for y^+>40 while PIV underestimates $\langle u^2\rangle/u_{\tau 0}$ closer to the wall. The latter is associated with the limited spatial-resolution of PIV in resolving the small-scale near-wall structures. The spatial-resolution issue is alleviated for polymer solutions since λ increases significantly with increasing polymer concentration (see Table 1). The first few data points at y^+<10 are expected to be erroneous as $\langle u^2\rangle$ does not converge to zero. This is mainly due to presence of mirrored particle images in the near-wall interrogations windows. The $\langle u^2\rangle$ peak is farther away from the wall for the polymeric solutions, which indicates a thicker buffer layer as it was also observed in the semi-log plot of Figure 4. Previous experiments also confirm that the location of the $\langle u^2\rangle$ peak moves away from the wall as the extent of DR increases[3, 8, 34, 35]. As discussed below, however, the variation of the peak value with increasing polymer concentration (or increasing DR) does not seem to follow a monotonous trend.

An analysis of the peak value of $\langle u^2 \rangle$ is conducted here for polymeric flows at constant flow rate. The variation of $\langle u^2 \rangle$ is also considered when normalized using the inner scaling of Newtonian flow ($u_{\tau 0}$) instead of the friction velocity of each polymer solution. This is applied to avoid variation of $\langle u^2 \rangle$ due to change in friction velocity at a similar flow rate. The value of the $\langle u^2 \rangle$ peak in Figure 5(a) increases by ~10% as the XG concentration increases and reaches maximum at 100 ppm of XG. When the polymer concentration is increased to 125 ppm, the peak value of $\langle u^2 \rangle$ is seen to reduce significantly, to the point that it is at approximately the same level as the Newtonian flow. Warholic et al.[3] used a polyacrylamide polymer (Separan AP-273) and divided their investigation to low (<35%) and high DR regimes. In the lower DR regime they observed an initial increase (~2%) of $\langle u^2 \rangle$ peak for 14% DR and another increase (~2%) of $\langle u^2 \rangle$ peak for 19% DR followed by a 4% decrease of non-normalized $\langle u^2 \rangle$ peak. At higher DR of 63%, they observed up to 60% reduction in the peak $\langle u^2 \rangle$ value. Wei et al.[34] observed about ±10% variation in peak $\langle u^2 \rangle$ value in DR range of 30 to 40% using PEO polymer. Escudier et.al.[8] also observed an increase of dimensional $\langle u^2 \rangle$ peak until 59% DR followed by a sudden large reduction at 67% DR for XG polymer solution at high concentrations (300 to 1500 ppm).

The peak value of $\langle u^2 \rangle$ for all polymer solutions is as large as the peak value for water. The value of $\langle u^2 \rangle^{0.5}$ (i.e., streamwise turbulence intensity) at the peak location is also about $0.15U_b$, which confirms the flow is still turbulent. Escudier et.al.[8] measured $\langle u^2 \rangle^{0.5}/U_b$ of about 0.02-0.03 in a laminar flow (Probably due to TS (Tollmien–Schlichting) waves) which increased up to 0.1 to 0.15 after transition to turbulent for a polymeric flow. These indicate that the flow field in all polymer solutions is turbulent.

The wall-normal component of normal Reynolds stress, $\langle v^2 \rangle$, normalized using $u_{\tau 0}$ are plotted as a function of the wall-normal distance y^+_0 in Figure 5b. The PIV measurements of $\langle v^2 \rangle$ in water agree with the DNS of Re_τ=180 at y^+>25. The overestimation in the near-wall is again associated with the presence of mirrored particle images. The $\langle v^2 \rangle$ profile and the peak value of each profile attenuate with increasing XG concentration. The location of the $\langle v^2 \rangle$ peak is also displaced away from the wall. The effect of polymer concentration on the peak $\langle v^2 \rangle$ value is observed to be non-linear as there is a large attenuation from water (Newtonian) to 75 ppm of XG followed by a slight reduction at 100 ppm, and another significant reduction at 125 ppm. The reduction of $\langle v^2 \rangle$ profiles with increasing drag reduction agrees with the results of Warholic et al.[3, 35] presented for both low

and high drag reduction regimes. They observed ~85% attenuation for 69% DR and also displacement of the peak location away from the wall. Wei et al.[34] observed ~40% reduction in the $\langle v^2 \rangle$ peak at 39% DR. Escudier et.al.[8] observed reduction of the $\langle v^2 \rangle$ peak with increase of XG ppm (also DR).

The profile of Reynolds shear stress, $\langle uv \rangle$, is shown in Figure 5c. The PIV measurement of $\langle uv \rangle$ at Re_τ=220 is not expected to overlap with the DNS data at Re_τ=180 since the wall shear stress is different. The slope of the $\langle uv \rangle$ profile at the centerline of the channel is also expected to decrease with increase of Re_τ as observed in Figure 5c. However, that PIV measurement underestimated $\langle uv \rangle$ peak since the peak for Re_τ=220 should be slightly larger than that of Re_τ=180. This is associated with the finite spatial resolution and correlation noise between u and v components. The peak value reduces with increasing polymer concentration while the peak location monotonously shifts away from the wall. Warholic et al.[3] also observed attenuation and displacement of $\langle uv \rangle$ peak away from the wall with the increase of the drag reduction. They observed up to 94% reduction of the $\langle uv \rangle$ peak at 69% DR. The measurements of Wei et al.[34] demonstrated ~54% reduction in the peak $\langle uv \rangle$ at 39% DR. In addition, Escudier et.al.[8] observed $\langle uv \rangle$ decreases with increasing DR; in fact they reported that the Reynolds shear stresses essentially become negligible at 67% DR.

The DNS of Tsukahara et al.[1] at Re_τ=70 is also presented in Figure 5 in order to evaluate the effect of reduction in Re_τ. This DNS data is normalized using the $u_{\tau 0}$ used for normalization of the polymer flows. The peak value of $\langle u^2 \rangle$, $\langle v^2 \rangle$ and $\langle uv \rangle$ for Newtonian DNS at Re_τ=70 is significantly smaller than those of XG-125 at Re_τ=67. This indicates that the observed trends is not due to the variation of Re_τ. In fact, the Newtonian flow at Re_τ = 70 is laminar while the flow of XG-125 at Re_τ = 67 is still turbulent.

The analysis of the results of the present study and comparison of these results with those reported in the literature both indicate that when polymer drag reduction occurs, the peaks of the normal and shear Reynolds stresses move away from the wall, indicating a thicker viscous sublayer and buffer layer. There also is a consistent reduction of $\langle v^2 \rangle$ and $\langle uv \rangle$ with increasing DR. The current results and some previous experiments (Warholic et al.[3] and Escudier et.al.[8]) show the same trend in variation of $\langle u^2 \rangle$ with DR percentage. The presence of large $\langle u^2 \rangle$ and small $\langle v^2 \rangle$ at maximum DR show a larger anisotropy compared to Newtonian turbulent channel flow.

(a)

(b)

(c)

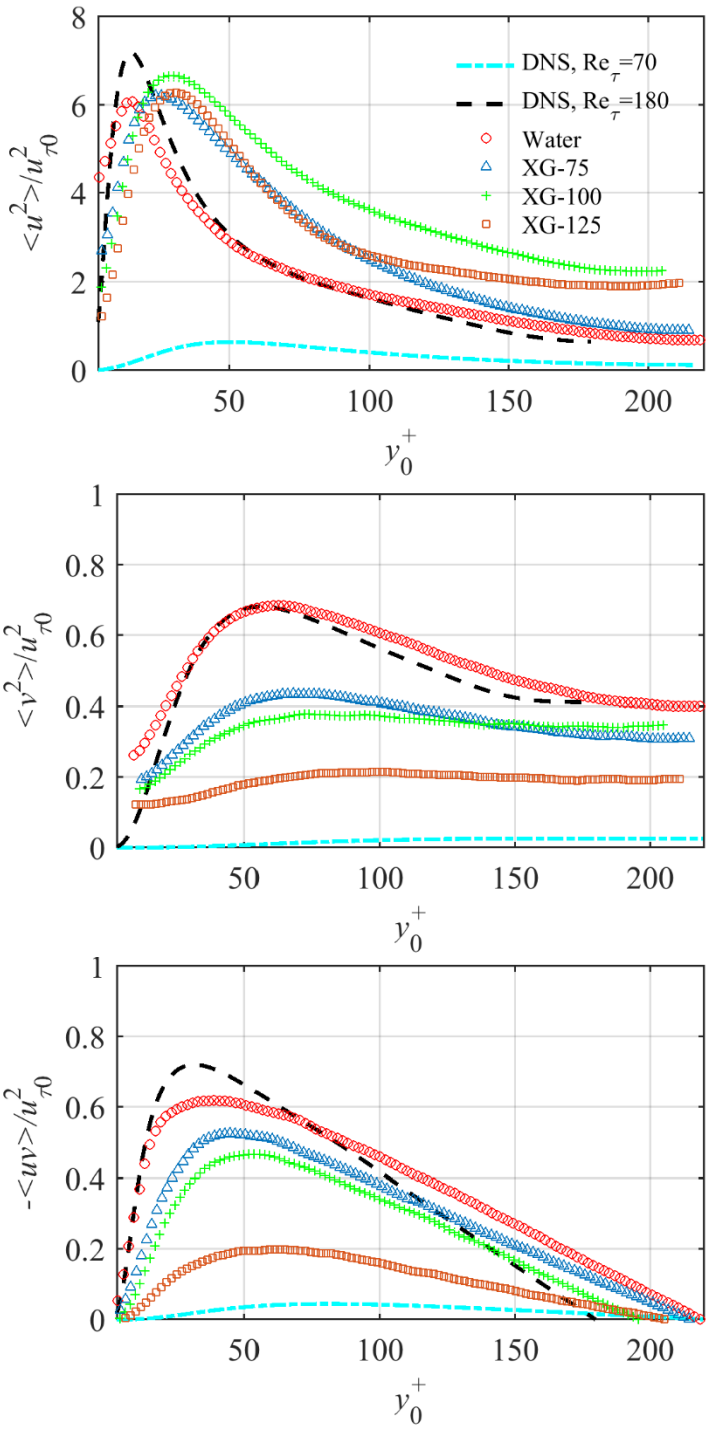

FIG. 5. The effect of XG polymer concentration on the (a) streamwise (b) wall-normal, and (c) shear Reynolds stresses normalized by the reference friction velocity of water ($u_{\tau 0}$) and plotted against wall-normal distance normalized by the reference inner scale (λ_0). The DNS of Newtonian channel flow by Tsukahara et al.[32] at Re_τ= 180 is provided to evaluate the uncertainties of PIV measurement in water at Re_τ= 220. This DNS data is normalized with its corresponding friction velocity ($u_{\tau 0}$) at Re_τ= 180. The DNS data of Tsukahara et al.[32] at Re_τ= 70 is also presented to investigate the effect of Re_τ variation of polymeric flows. This DNS data is normalized using $u_{\tau 0}$ at Re_τ= 220 similar to the polymer flows. Both DNS data are presented for channel height of the current experiment.

C. High-order turbulence statistics

The triple products of velocity fluctuations can identify the direction of the transport of turbulent kinetic energy. The transport of streamwise component of turbulent kinetic energy (i.e., $\langle u^2 \rangle$) by u and v velocity fluctuations for XG-75, 100, and 125 ppm is demonstrated in Figure 6 (a), (b), and (c), respectively. The triple products and the wall-normal distance are normalized by the reference friction velocity ($u_{\tau 0}$) and wall unit (λ_0) of the Newtonian flow. The triple products from PIV measurements of water flow and also $\langle u^3 \rangle$ from the simulations of Iwamoto et al.[36] at Re_τ = 150 and 300 are presented in all plots for comparison. Although the trend of $\langle u^3 \rangle$ for water is similar to that obtained from the simulations, the magnitudes are different due to the smaller aspect ratio of the channel and the spatial averaging of the PIV. The near-wall peak in the DNS profiles, which occurs at about $y^+_0 \sim 7$, is not seen in the PIV data for water due to finite spatial resolution and signal truncation within the near-wall interrogation windows.[37] The lack of near-wall peak of $\langle u^3 \rangle / u_{\tau 0}^3$ for XG-75 is also associated with bias error of PIV in the near wall region ($y^+_0 < 10$). However, the near-wall peak is away from the wall and out of the biased error region of PIV for the solutions with higher polymer concentrations (XG-100 and XG-125), as it is observed at $y^+_0 \sim 15$ and 25 in Figure 6 (b) and (c), respectively.

The positive values of $\langle u^3 \rangle / u_{\tau 0}^3$ and small negative values of $\langle u^2 v \rangle / u_{\tau 0}^3$ in the near wall region of $y^+_0 < 13$ show the dominance of the sweep events ($u > 0$, $v < 0$), while the negative value of $\langle u^3 \rangle / u_{\tau 0}^3$ and the positive value of $\langle u^2 v \rangle / u_{\tau 0}^3$ indicate the dominance of ejection events ($u < 0$, $v > 0$) at $y^+_0 > 13$ for the Newtonian flow. The transition between these two sweep and ejection dominated regions is indicated by the solid (red) vertical line in Figure 6. This transition line for the XG-75 solution is indicated by dashed (blue) vertical line, which is displaced farther from the wall to $y^+_0 = 20$. The local minimum of $\langle u^3 \rangle / u_{\tau 0}^3$, which shows strong ejection motions, intensifies and is also displaced from the wall for XG-75. A similar shift of $\langle u^2 v \rangle / u_{\tau 0}^3$ peaks away from the wall is observed for XG-75 although the magnitudes are smaller. Wei et al.[35] investigated the skewness of u, defined as $\langle u^3 \rangle / \langle u^2 \rangle^{3/2}$, for different polymer solutions with DR in the range of 30-40%. Their results showed that the transition between the sweep dominated region in the immediate vicinity of the wall and the ejection dominated region occurred at $y^+_0 \sim 20$. They also observed that the negative peak is intensified and displaced from the wall with increasing DR. The presence of these two regions was also observed by Warholic et al. [36].

The transport mechanism of $\langle u^2 \rangle$ for XG-100 in Figure 6(b) is similar to that of XG-75 while the transition between sweep and ejection (vertical dashed line) is shifted farther from the wall to y^+_0=34. The positive $\langle u^3 \rangle$ peak for XG-100 is found at y^+_0=15 while the negative $\langle u^3 \rangle$ peak intensifies and shifts farther from the wall compared to XG-75. The negative and positive peaks of $\langle u^2 v \rangle$ for XG-100 are also displaced away from the wall. The positive $\langle u^3 \rangle$ peak for XG-125 in Figure 6(c) has significantly intensified and moved away from the wall to y^+_0= 25. The transition of sweep and ejection regions occurs at y^+_0=80. There is no negative peak in $\langle u^3 \rangle$ profile of XG-125 while the negative values extend to the channel centerline. The trend of $\langle u^2 v \rangle / u_{\tau 0}^3$ for XG-125 is the same as that of XG-75 and XG-100 while the relatively small peaks are farther shifted away from the wall.

The increase in XG concentration (and consequent increase in DR) has resulted in the extension of the end of the sweep dominated region from y^+_0= 13 (Newtonian) to y^+_0=80 (XG-125), where an ejection dominated region starts. The intensity of the positive $\langle u^3 \rangle$ peak also increases with increasing polymer concentration which indicates stronger positive *u* fluctuations. The core of the ejection dominated region (i.e., negative peak of $\langle u^3 \rangle$) shows the center of the buffer layer (y^+_0~20) for the water results. The negative peak of $\langle u^3 \rangle$ is displaced away from the wall for XG-75 and XG-100 while it has almost disappeared for XG-125. The $\langle u^3 \rangle$ profile in Figure 6 also allows for the investigation of the degree of asymmetry in the distribution of *u* fluctuations. The increase in XG concentration (and DR) has resulted in larger positive *u* fluctuations in the near wall region while the negative *u* fluctuations seem to attenuate and are displaced toward central region of the channel. However, evaluation of the fourth order moment (i.e., flatness) is required to identify if the larger positive/negative $\langle u^3 \rangle$ peak is caused by a large number of small *u* fluctuations or a smaller number of intense *u* fluctuations.

As shown in Figure 7, the peak value of $\langle u^4 \rangle / u_{\tau 0}^4$ is assumed to be at about y^+_0~15 for water which indicates presence of *u* fluctuations with larger amplitude. The near-wall data (y^+_0<10) are not shown due to the effects of significant bias error in the fourth-order moment. The peak location of $\langle u^4 \rangle$ has moved to y^+_0~28 for all XG concentrations. The magnitude of $\langle u^4 \rangle$ increases with increasing polymer concentration, indicating presence of a greater number of intense positive *u* fluctuations.

(a)

(b)

(c)

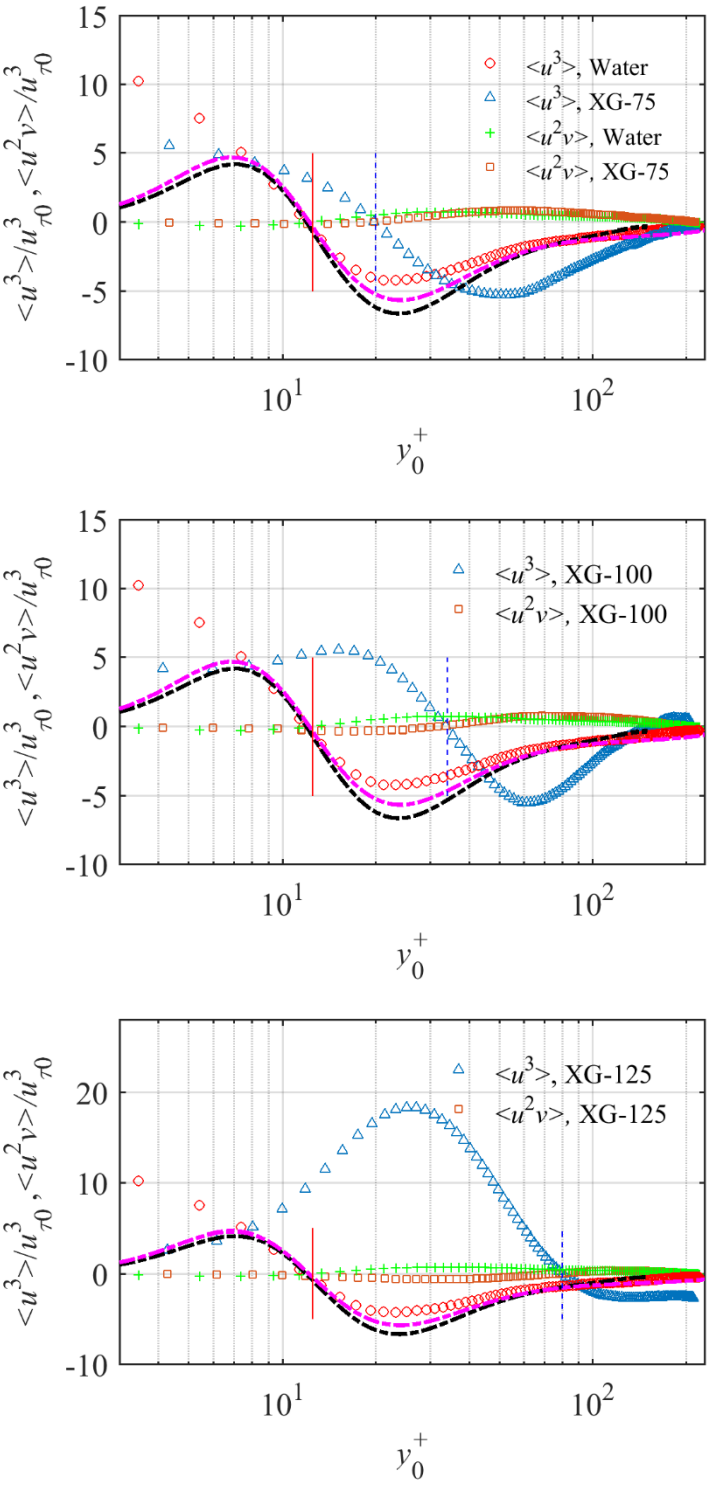

FIG. 6. The triple products of u and v calculated to investigate the transport direction of streamwise turbulent kinetic energy. Profiles of $\langle u^3 \rangle$ and $\langle u^2 v \rangle$ for (a) XG-75 (b) XG-100, (c) XG-125 are shown. Profiles of $\langle u^3 \rangle$ from DNS of Iwamoto et al.[36] at Re_τ = 150 (---) and 300 (-·-·-) and PIV measurement in water are also shown for comparison. The vertical solid (red) and dashed (blue) lines indicate the location of transition from a sweep dominated to an ejection dominated region for water and polymer solution, respectively.

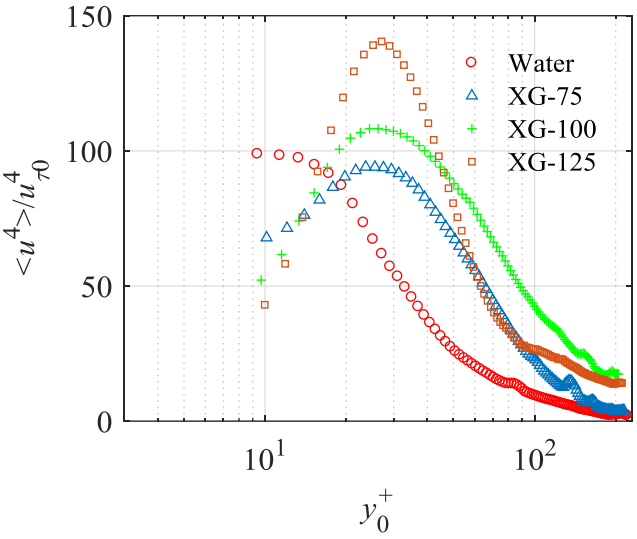

FIG. 7. Profiles showing $<u^4>/u_{\tau 0}^4$ for water and polymer solutions.

D. Quadrant of turbulent fluctuations

The contribution of ejection and sweep motions to total turbulence production is investigated using conditional averaging of the Reynolds shear stress, $<uv>$, based on the sign of u and v fluctuations.[38] The conditional average is indicated as uv_{Qi} where i varies from 1 to 4 referring to the four quadrants of the u vs v plot in the counter clockwise direction. Figure 8 demonstrates uv_{Qi} normalized with the reference (water) friction velocity. It should be noted that uv_{Q2} and uv_{Q4} have a negative sign and result in turbulence production, while uv_{Q1} and uv_{Q3} events with a positive sign result in damping turbulence production.[39]

The conditional average of the uv_{Q1} in Figure 8a shows the contribution of $u>0$ and $v>0$ fluctuations to $<uv>$. In the near wall region ($y^+_0<13$), uv_{Q1} decreases with increasing XG concentration. Within the layer $13<y^+_0<80$, uv_{Q1} increases with increasing polymer concentration. There is also a positive peak in this region which becomes more pronounced and moves away from the wall at higher polymer concentrations. At $y^+_0>80$, the XG-100 solution has the largest value of uv_{Q1} of the 3 polymer concentrations tested

In Figure 8b, the profiles of uv_{Q2} are shown. Recall that uv_{Q2} is associated with ejection, a major contributor to turbulence production. Generally, as can be seen in Figure 8b, the intensity of ejection motions increases with increasing wall normal distance, reaches a maximum, and

decreases gradually until the centerline of the channel is reached. The peak value of uv_{Q2} is attenuated with increasing XG concentration and the location of the peak moves away from the wall. The magnitude of uv_{Q2} decreases with increasing XG concentration, implying the reduction of turbulence production due to ejection.

Figure 8c shows that uv_{Q3} events decrease with increasing XG concentration in $y^+_0 \leq 35$, which results in increasing turbulence production. It should be noted that the value of uv_{Q3} for XG-125 is less than water in $y^+_0 \leq 100$. The location of the maximum peak of uv_{Q3} events moves away from the wall for XG-75 and XG-100, while the peak disappears for XG-125. For the regions far away from the wall, the value of uv_{Q3} of polymer solution is greater than water, showing the reduction of turbulence production for polymer solution.

Values of uv_{Q4}, shown in Figure 8d, indicate the contribution of sweep motions to turbulence production. For water, values of uv_{Q4} decrease with increasing wall normal distance for $y^+_0 \leq 10$, stays constant until about $y^+_0 = 50$ followed by a gradual reduction until the channel centerline. In the vicinity of the wall (i.e. within the region $y^+_0 < 15$), an increase in XG concentration results in smaller contribution of sweep events to the total Reynolds stress. The uv_{Q4} profile for the XG-75 solution follows a similar trend as was observed for water but the values are attenuated across the channel. However, further increases in XG concentration produce larger values of uv_{Q4} in the region $15 < y^+_0 < 100$.

The results for water, shown in Figure 8, confirm the dominance of sweep events at $y^+_0 < 13$ and then the greater contribution of ejection to Reynolds shear stress at $y^+_0 > 13$. This is in agreement with the results of Kim et al.[39] that showed this transition from sweep-to-ejection occurs at about $y^+_0 = 12$ for Newtonian flows. Evaluation of the uv_{Qi} in the four quadrants shows that the significance of ejection is significantly reduced in the polymeric solutions relative to the Newtonian (water) flow. A consistent reduction of contribution of ejection was observed in Figure 8b with increase of ppm (increase of DR). The second largest contributor to the Reynolds shear stress (i.e., sweeps) also appear to attenuate at the near-wall region ($y^+_0 < 13$) with increase of DR. The sweeps also appear to initially attenuate with increase of polymer concentration at about $y^+_0 \sim 40$ while they intensify at the maximum DR (which was obtained with the XG-125 polymer solution).

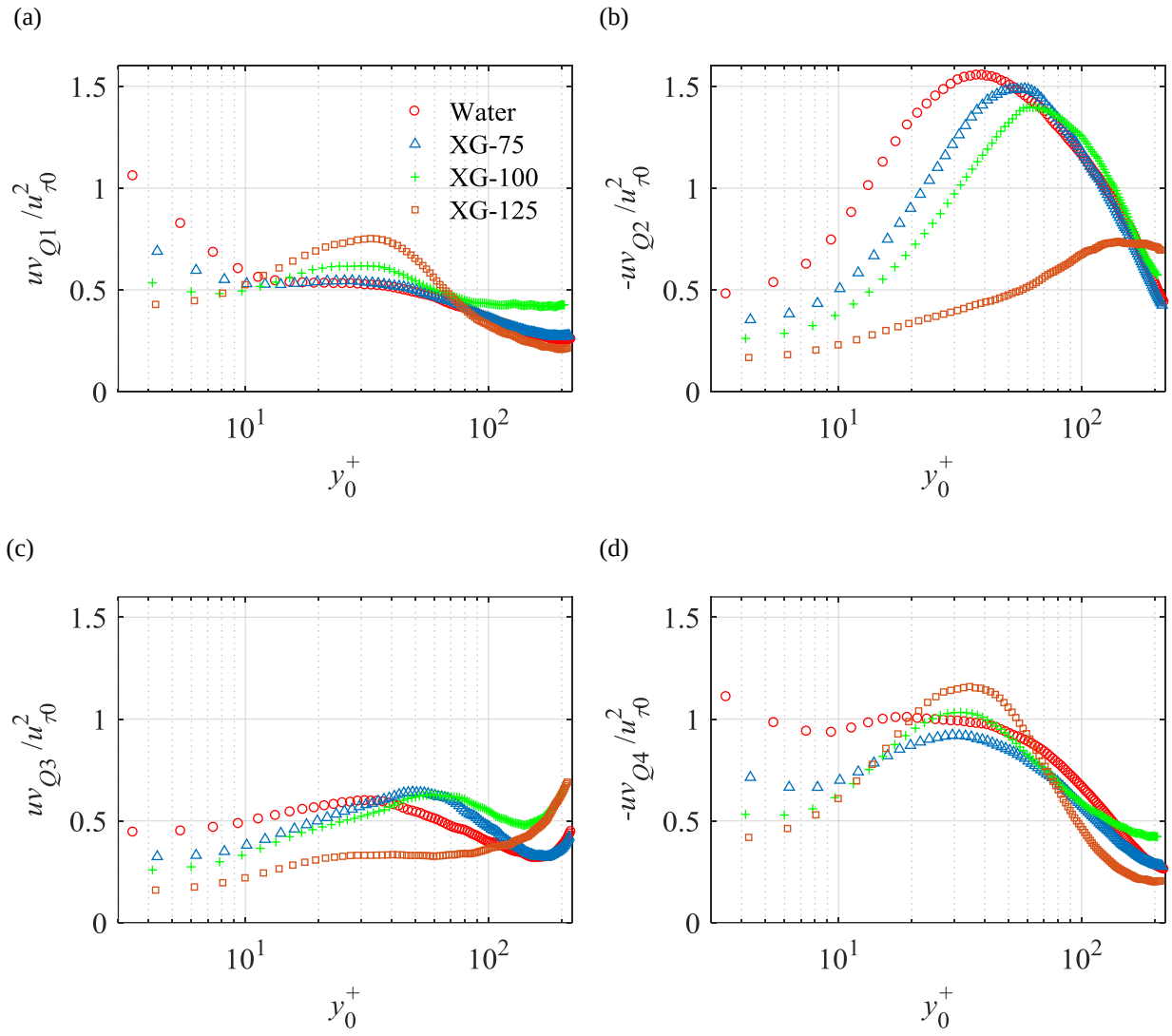

FIG 8. Evaluation of the conditional averages of the four quadrants (a) uv_{Q1}, (b) uv_{Q2}, (c) uv_{Q3}, and (d) uv_{Q4}.

The effect of XG polymer concentration on turbulent fluctuations is further investigated using joint probability density functions (i.e., quadrant analysis) determined at two wall-normal locations. The results are presented in Figure 9. The first location was chosen at y^+_0=25 to investigate the turbulence at the positive peak location of $<u^3>$ for XG-125 in Figure 6c. The second location , y^+_0=140, is in the outer layer.

Figures 9a and b show that the JPDF in the second (ejection) and fourth (sweep) quadrants are larger than the first and third quadrants for the water flow. The positive and negative u velocity fluctuations become weaker with increasing wall-normal distance (Figure 9b) while the positive

and negative *v* velocity fluctuations approximately have the same magnitude. The angle of the ejection/sweep motions (principal axis of Reynolds stress tensor) with respect to the wall becomes larger as the wall-normal distance increases. In addition, the sweeps of the fourth quadrant occupy a smaller area at y^+_0=140, which indicates attenuation of intense sweep motions.

The quadrant analysis of the flow of the XG-75 solution, presented in Figures 9c and d, show reduction of the magnitude of *v* fluctuations and increase of the strength of *u* fluctuations in both wall-normal locations in comparison with the Newtonian flow. The same trend is also observed for the XG-100 solution, shown in Figures 9e and f. As a result, the angle of principal axis of the Reynolds stress tensor with respect to the wall decreases, which shows shallower sweep/ejection motions at y^+_0=25.

The JPDF analysis shows a different pattern of turbulence fluctuations at the point of MDR (obtained with the XG-125 solution). These results can be found in Figures 9g and h. The magnitude of *v* fluctuation has further decreased at both wall-normal locations relative to the XG-75 and XG-100 cases, while *v* distribution remains symmetric. At y^+_0=25, a highly skewed distribution of *u* is observed. There is a large number of weak $u<0$ fluctuations at about $u/u_{\tau 0} = -2$ while there is a small number of $u>0$ fluctuations with maximum intensity of about $8u_{\tau 0}$. The principal axis is also almost horizontal which indicates a lack of inclined shear-layer found in Newtonian wall flows. At y^+_0=140 for XG-125 solution, the *u* fluctuations are still stronger than the *v* fluctuations. However, the distribution shows that stronger *u* fluctuations ($u > 3u_{\tau 0}$ or $u < -3u_{\tau 0}$) seems to occur along with positive *v*.

Walker et al.[40] and Fu et al.[41] observed a similar JPDF with symmetric contours with respect to the *u*-axis (i.e. symmetric *v* fluctuations) for a turbulent channel flow with flexible PAM and PEO polymers. Fu et al.[41] showed that the angle of the principal axis of shear stress with respect to the *u*-axis varies from -2º to -8º as y^+_0 varies from 50 to 200 for a channel flow with an average PEO polymer concentration of 14 ppm. This is a more acute (shallow) principal axis angle than that observed for water at the same Reynolds number (i.e., -8º to -18º). Kim et al.[42] also observed approximate alignment of the principal axes of Reynolds stresses with the *u*-axis. These investigations support the JPDF analysis presented here for the XG-75 and XG-100 solutions, as the results described above are associated with conditions where the point of MDR has not yet been reached, and exhibit considerable residual $\langle uv \rangle$ across the channel. The current investigation

depicts further skewness of u in JPDF at the MDR condition of XG-125. The skewness is characterized by a large number of small negative u fluctuation and small number of large positive u fluctuations at the y^+_0~25.

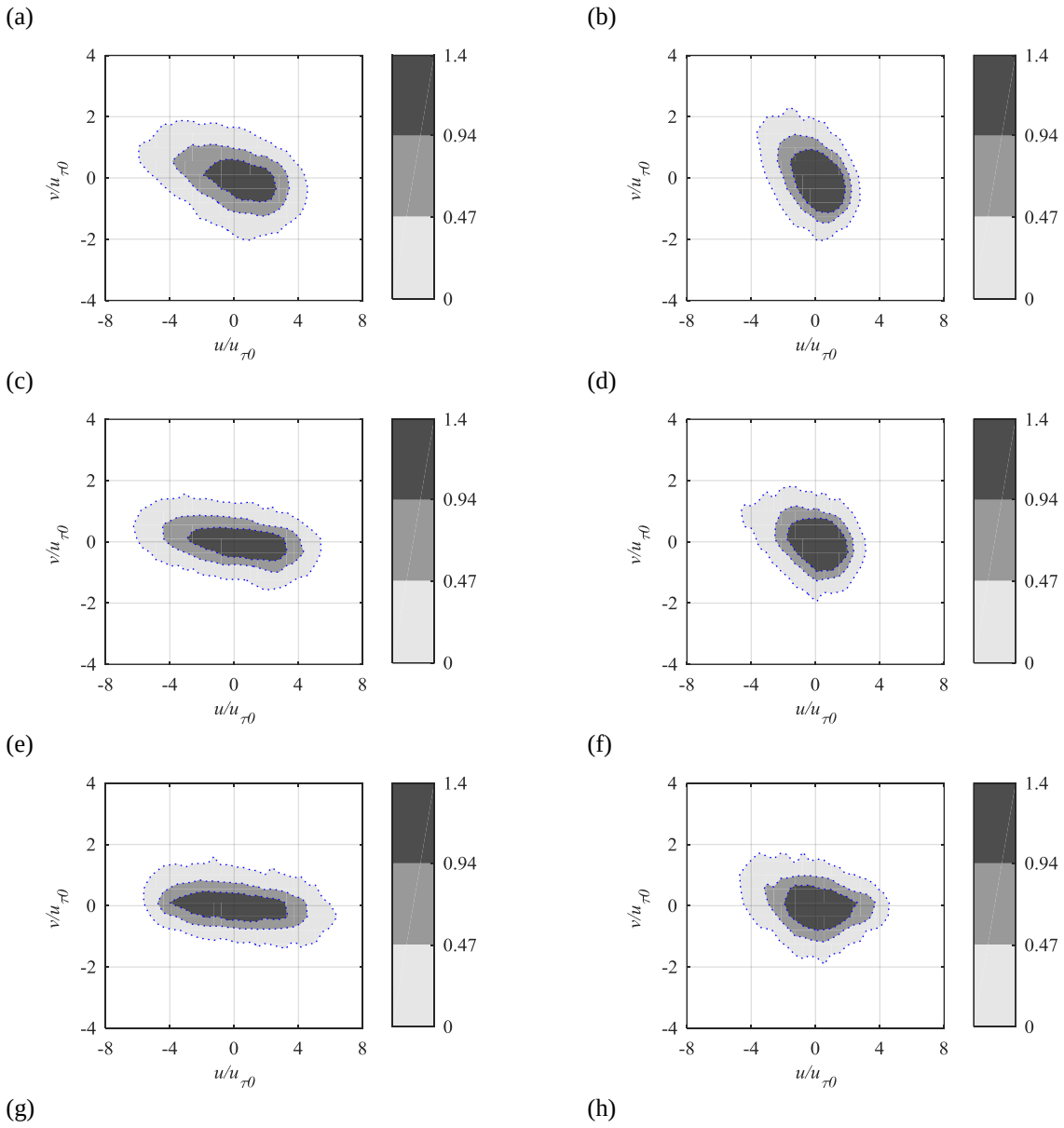

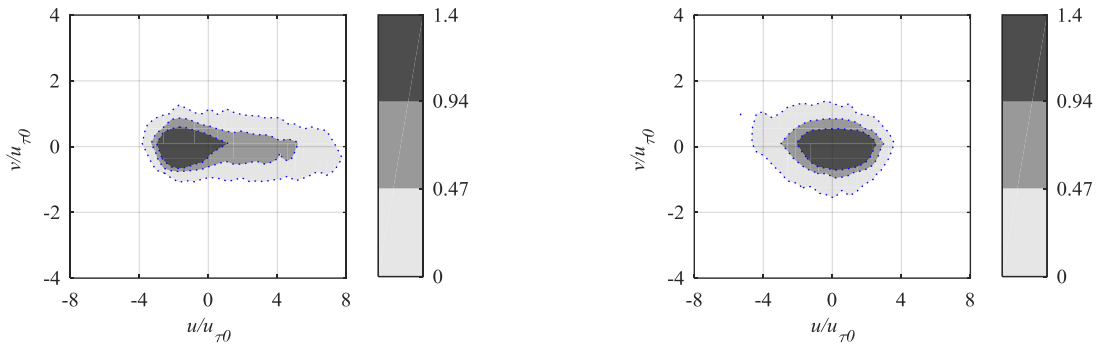

FIG 9. The JPDF of turbulent motions in water (a and b), XG-75 (c and d), XG-100 (e and f), and XG-125 (g and h). The figures on the left (a, c, e, and g) correspond to y^+_0 = 25 and the figures on the right (b, d, f, h) correspond to y^+_0=140.

E. Length scales of XG polymer solutions

The length scales of turbulent structures are analyzed here using spatial correlation. White et al.[43] showed that the polymer additives increase the spanwise spacing of the low and high speed streaks. However, it appears that length scales in channel flows of drag-reducing polymer solutions, in both the streamwise and wall-normal directions, have not been explored. The streamwise and wall-normal spatial-correlations of u and v are determined using

$$C_{u_i u_i,x} = \frac{< u_i(x, y_0) u_i(x + \Delta x, y_0) >}{< u_i(x, y_0)^2 >} \tag{2}$$

$$C_{u_i u_i,y} = \frac{< u_i(x_0, y) u_i(x_0, y + \Delta y) >}{< u_i(x_0, y)^2 >} \tag{3}$$

where x_0 and y_0 indicate the center point of spatial correlation while the index i refers to u (i=1) and v (i=2). Figures 10a and 10b show $C_{uu,x}$ at y^+_0 =25 and 140 for water and for the XG solutions. The streamwise displacement (Δx) is normalized based on the wall unit ($\delta x^+_0=\Delta x/\lambda_0$). The spatial-correlation in the x direction increases with increasing XG concentration, implying longer streamwise coherence of the turbulent structures. Figures 10c and 10d demonstrate that the streamwise coherence of v is smaller than u for both the water and polymer solutions. It is also observed in Figure 10c that at y^+_0=25, $C_{vv,x}$ attenuates with polymer concentration. Therefore, the length scale of v fluctuations becomes smaller in the x direction with increasing DR. The spatial-

correlation at y^+_0= 140, shown in Figure 10d, indicates larger streamwise length scales of *v* fluctuations for the XG-75 and XG-100 solutions relative to water. The XG-125 solution shows a sudden reduction of $C_{vv,x}$ for $\delta x^+_0 < 20$ followed by a gradual reduction beyond this point.

Figures 11a and 11b present wall-normal spatial-correlations of *u* and *v* fluctuations. In Figure 11a, it can be seen that the $C_{uu,y}$ profile shows increasing spatial coherence of *u* fluctuations in the *y* direction with an increase of XG concentration from 75 to 100 ppm. A further increase to 125 ppm results in formation of alternating low and high speed streaks (or layers) in the wall-normal direction since $C_{uu,y}$ changes sign at y^+_0=50 and 150. The distance between the center of alternative positive and negative *u* layers is estimated to be about 75-100λ_0. The spatial-correlation of *v* in the *y* direction, as shown in Figure 11b, is approximately the same for water and XG-75 and XG-100, while there is a sudden reduction of wall-normal length scales for XG-125 solution.

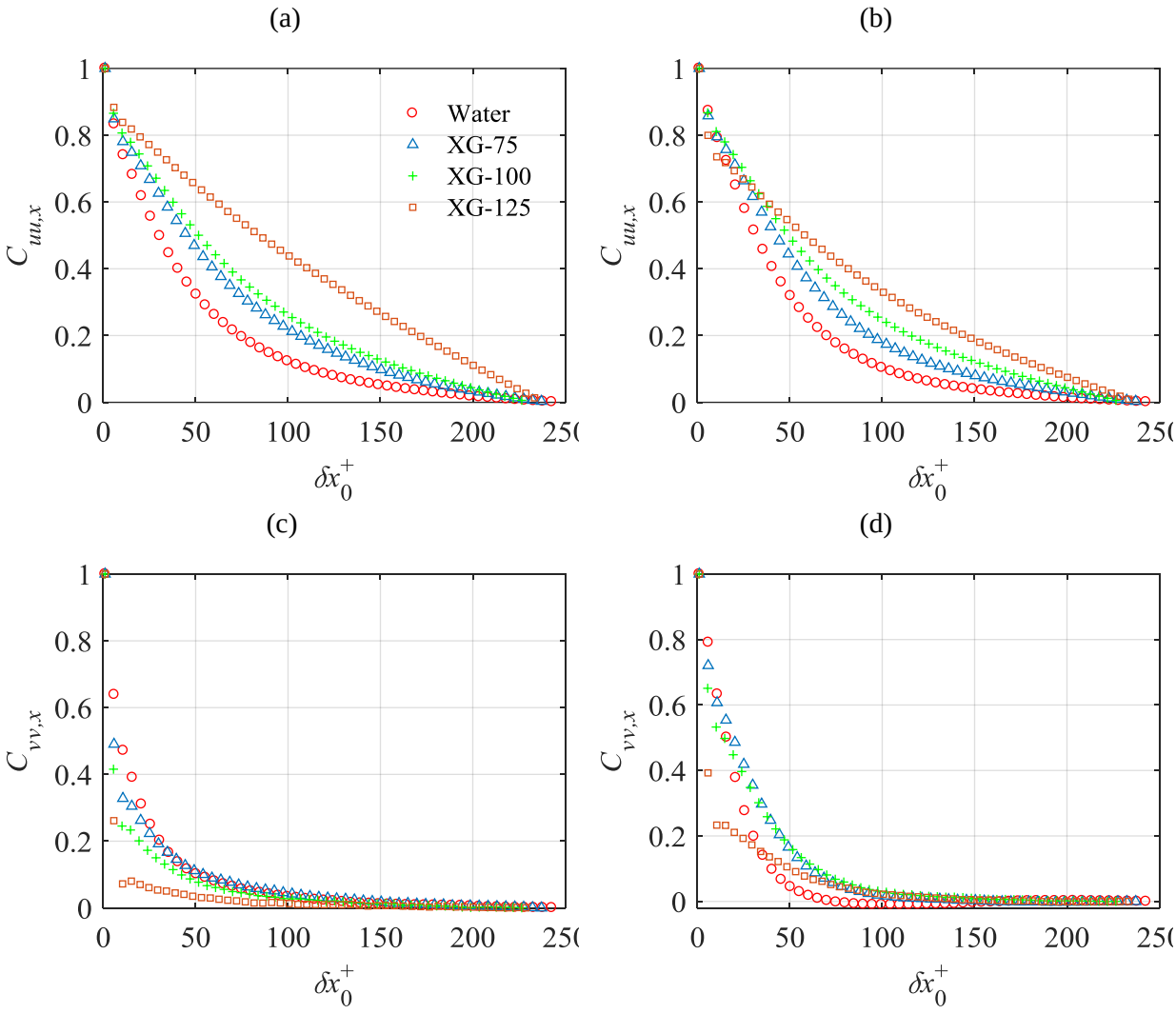

FIG 10. Spatial-correlation of streamwise (a and b) and wall-normal (c and d) in the *x* direction. Two wall-normal locations of y^+_0 =25 (a, c) and y^+_0 =140 (b, d) are shown. Only one out of five data points is presented for clarity.

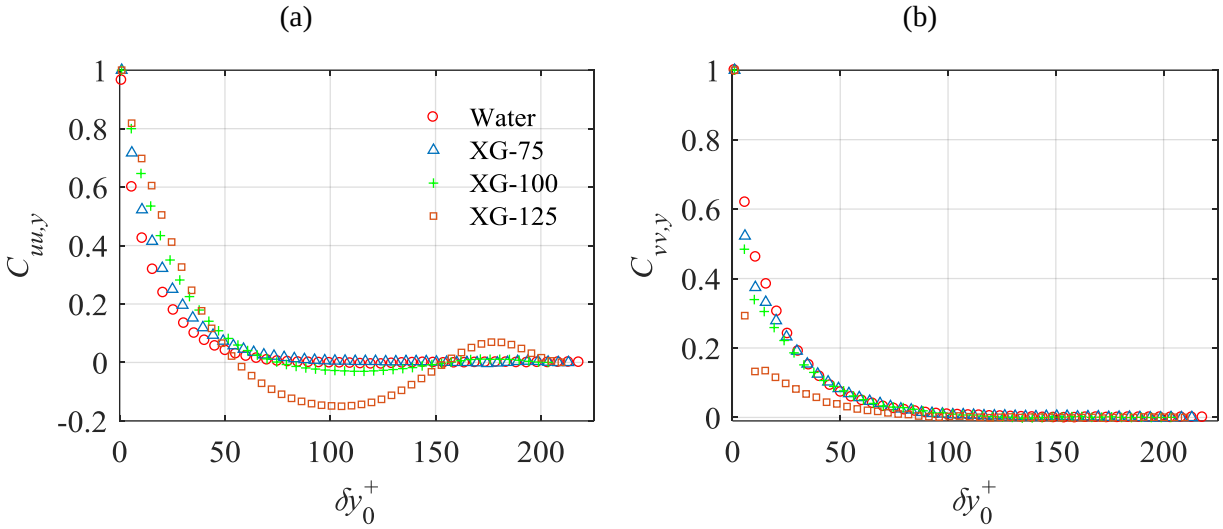

FIG 11. The effect of XG concentration on the spatial correlation of (a) streamwise and (b) wall-normal fluctuations in the *y* direction. Only one out of five data points is presented for clarity.

F. Spatial organization of energetic modes

The POD method decomposes the velocity fluctuation field to the dominant eigenmodes, which present spatial description of turbulent structures carrying most of the flow energy.[44, 45] The snap-shot POD method is applied here to a half-channel domain (from the wall to the centerline) based on the algorithm proposed by Lumley et al.[45] and Meyer et al.[46]. The velocity fluctuations are decomposed into a sum of modes and temporal coefficients as follows:

$$u(x,t) = \sum_{k=1}^{N} a^k(t)\phi^k(x) \qquad (4)$$

where $u(x,t)$, N, $a^k(t)$, and $\varphi^k(x)$ are the velocity fluctuations, the number of snapshots, time coefficient, and normalized modes, respectively . The *u* and *v* fluctuations are appended into one matrix followed by forming an autocovariance matrix. The eigenvalues are ordered in descending order and the energy of each mode is determined by its eigenvalue normalized by the sum of all eigenvalues.[46] The modes are normalized as

$$\phi^i = \frac{\sum_{n=1}^{N} A_n^i u^n}{\left\| \sum_{n=1}^{N} A_n^i u^n \right\|}, \quad i = 1, 2, ..., N. \tag{5}$$

where A^i_n is the nth component of the eigenvector corresponding to the relevant eigenvector. Figure 12 demonstrates the energy distribution for the first twenty modes. The first two modes of velocity fluctuations are dominant for water and the polymer solutions. The energy of the first two modes increases with the increasing polymer concentration. The two modes comprise 28% of the total turbulent kinetic energy for water while for XG-125 they represent 61% of the total energy. Each of the remaining modes have a smaller energy (< 4%) for water and the polymer solutions.

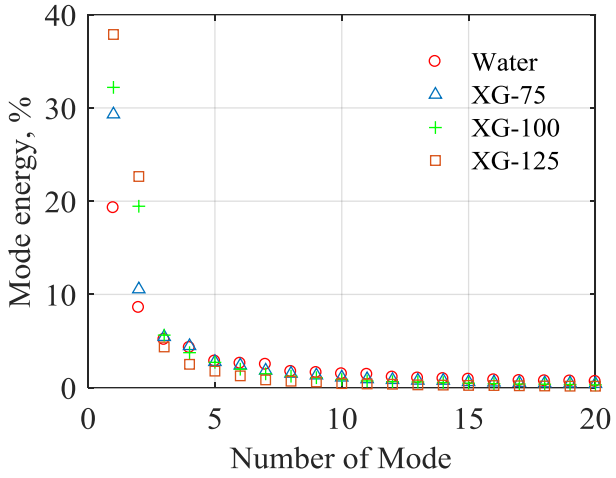

FIG 12. POD mode analysis for water and the XG polymer solutions.

The first two dominant modes are shown in Figure 13 for water and polymer solutions. It should be noted that the POD modes only describe the spatial pattern of the energetic modes and the sign of $a^k(t)$ coefficient for each snap-shot has to be taken into account in interpreting the direction and detailed description of the coherent motions. The first mode for water in Figure 13a captures large-scale ejection or sweep of fluid depending on the sign of the $a^1(t)$. The second mode in Figure 13b resembles the shear layer structure of Newtonian flows assuming a negative $a^2(t)$. The reverse vectors of this mode (i.e. $a^2(t) < 0$) show a strong ejection motion opposed by a sweep motion from the core of the channel. The interaction of the ejection and sweep motions results in the formation of a shear layer.[47] The angle of the shear layer at $y^+_0 = 20$ is about 8° with respect to the channel

wall which is in good agreement with the value (= 10º) reported by Kreplin et al.[48,49] The first and second modes of the XG-75 solution are similar to those of water. However, the angle of the shear layer is smaller. The trend continues for XG-100, as shown in Figure 13e and f, as weaker ejection or sweep is present in the first mode and the angle of the shear layer becomes smaller. At the point of MDR (i.e. for the XG-125 solution), the two modes are both horizontal with no indications of an inclined shear layer. An intense sweep or ejection motion (depending on the sign of $a^1(t)$) is observed in the first mode which uniformly spans the whole field-of-view. The second mode of XG-125 also shows a strong horizontal shear layer at about $y^+_0 \sim 50$. These modes indicate presence of layers of low and high streamwise momentum which are elongated in the *x*-direction at the MDR limit. Cai et al.[50] also showed that the first POD mode captures ejection of low momentum fluid and sweep of high momentum fluid, and the inclination angle of 30 ppm cetyltrimethyl ammonium chloride (CTAC) solution is smaller than that of water. Their results indicated that the second mode captured the ejection of low momentum fluid. The current study confirms the reduction of the inclination angle of the coherent structures during drag reduction and the presence of horizontal shear layers between low and high speed fluid at the MDR.

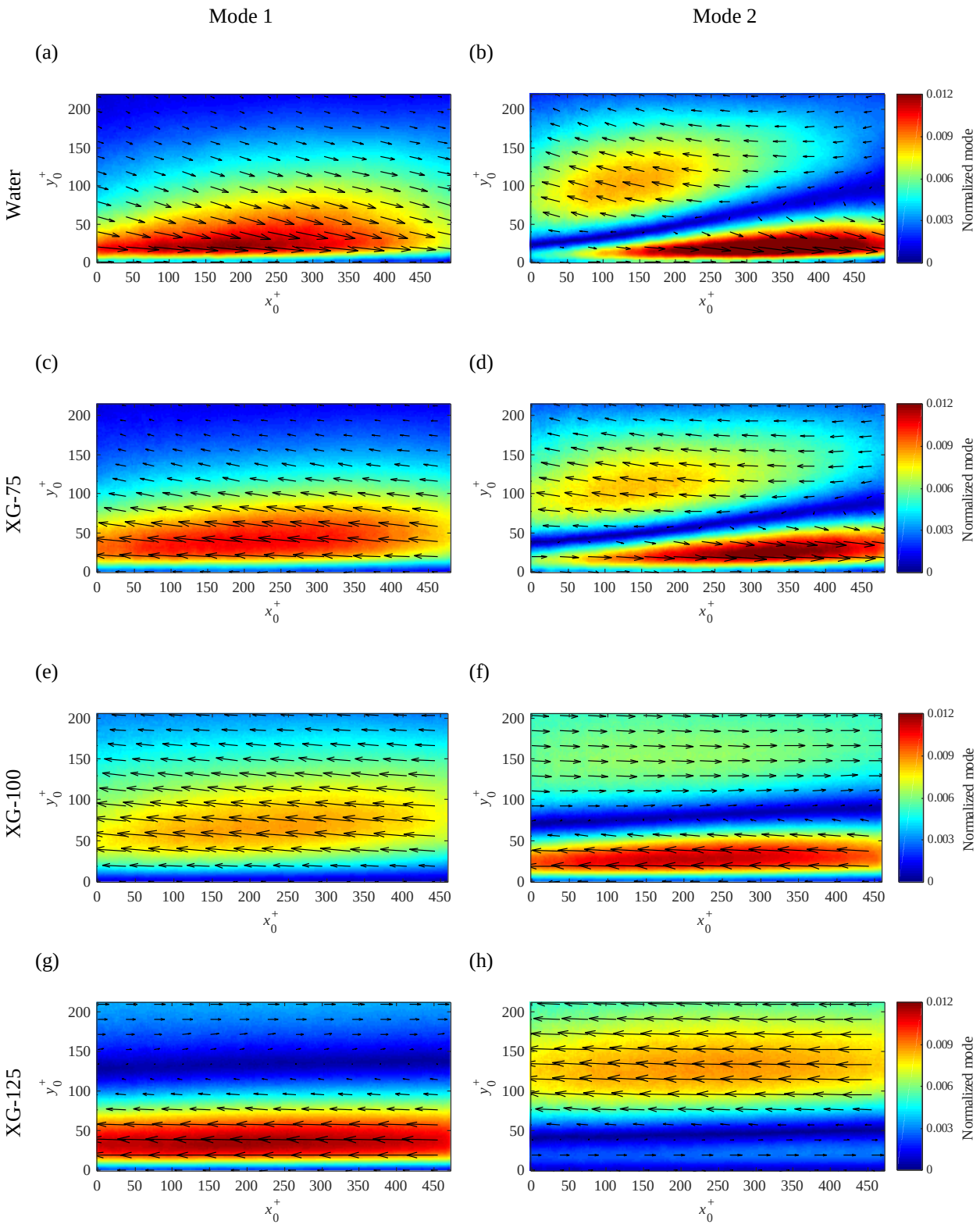

FIG 13. Dominant first and second POD modes for (a, b) water and polymer solutions of (c, d) XG-75, (e, f) XG-100, and (g, h) XG-125.

IV. SUMMARY AND CONCLUSION

The addition of rigid XG polymer to water at different concentrations has resulted in significant changes in the turbulent structures measured during channel flow at Re = 7200. There is a monotonic change of turbulence statistics with increasing polymer concentration, with turbulence production at a minimum when the point of maximum drag reduction (MDR) is reached. The investigations of the present study showed that the logarithmic layer, where turbulence production is balanced by the viscous dissipation of turbulence, shifts away from the wall with increasing XG concentration. This shift of the logarithmic layer is associated with reduction of near-wall turbulence production at all DR cases. The semi-log profile of mean velocity prior to MDR, falls between the Newtonian log-law and MDR profiles. This is in contrary to most of the previous observations of flexible polymers, which have a crossover point from MDR asymptote in the near-wall to a profile parallel to Newtonian log-law. At the MDR condition, turbulence production is so small that the logarithmic layer disappears and mean velocity follows Virk's asymptote[31]. The reduction of turbulence production is mainly is associated with changes in ejection motions (second quadrant of u-v plot) although there is a small increase of turbulence production by sweep motions (fourth quadrant, as shown in Figure 8d). At the MDR, streamwise Reynolds stress is as large as that of the Newtonian flow. This is in contrary to flexible polymers showing significant reduction of streamwise Reynolds stress at MDR. Wall-normal and shear Reynolds shear stresses of XG solution were also significantly attenuated which agrees with the trend of flexible polymers.

Investigation of the triple products of velocity fluctuations showed that the narrow sweep-dominated region in the immediate vicinity of the wall extends farther away from the wall with increasing polymer concentration. The outer boundary of the sweep-dominated layer moves from $13\lambda_0$ in the Newtonian flow to $80\lambda_0$ at MDR. The asymmetric behavior of positive u fluctuations (i.e., positive $\langle u^3 \rangle$) increases with increasing polymer XG concentration. This positive skewness ($\langle u^3 \rangle / \langle u^2 \rangle^{3/2}$) extends in the wall-normal direction and intensifies at larger DR values. The largest positive skewness is observed at MDR at $y^+_0 \sim 25$ where the largest flatness (Kurtosis or $\langle u^4 \rangle / \langle u^2 \rangle^2$) of u fluctuations is also observed.

The quadrant analysis at $y^+_0=25$ shows that the addition of polymers inclines the principal axis of v versus u plot from about 15 degrees (clockwise with respect to negative u-axis) in the Newtonian flow to almost zero (horizontal) at MDR. The JPDF of fluctuations becomes symmetric with

respect to the u axis at MDR. A large number of negative and weak u fluctuations ($-3u_\tau < u < -u_\tau$) along with a relatively smaller number of positive larger u fluctuations ($u > 6u_\tau$) are observed at MDR. The spatial-correlation of the fluctuating velocity field shows that an increase in XG concentration increases the spatial coherence of u fluctuations in the x-direction while v fluctuations are not affected and stay localized. The length scales of streamwise velocity fluctuation in wall-normal direction show the formation of low and high speed streak. Proper orthogonal decomposition (POD) confirms the results of the length scales of streamwise velocity fluctuation in wall-normal direction. The first energetic mode at MDR (obtained with 125 ppm XG polymer) shows streamwise elongated layers with positive and negative u fluctuations. The inclined shear layer structure of Newtonian wall flows, which plays a major role in turbulence production, is not present in the energetic POD modes of the flow at MDR.

AKNOWLEDGEMENTS

The authors gratefully acknowledge financial support provided by Natural Sciences and Engineering Research Council of Canada (NSERC), Alberta Innovates-Technology Futures (AITF), and the Donald Lougheed Engineering Graduate Scholarship.

APPENDIX

The velocity fields from PIV is used to analyze the distribution of energy in wavenumber ($k=2\pi/\lambda$, where λ is wavelength) domain for the Newtonian and the non-Newtonian solutions. The power spectral density (PSD) of streamwise velocity versus k at $y^+=25$ is shown in Figure 14. The PSD of water flow has larger energy and distributed over a wide range of wavenumber within the dynamic spatial range of the PIV system. The additional of the polymers has reduced the energy content of all the wavenumbers while the broadband shape of the PSD is maintained. There is no appearance of a peak potentially due to Tollmien-Schlichting instabilities as the polymer concentration is increased.

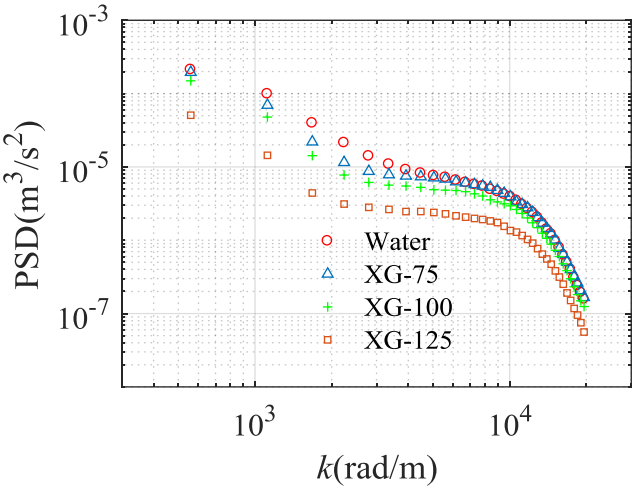

FIG 14. PSD of water and polymer solutions at y^+=25.

Statistical convergence of second and higher order turbulence statistics at y^+_0 =25 is carried for flow of water and XG-100 solution in Figure 15. Most of the statistics reach a plateau after about 4,000 PIV data points. The random error is calculated as the standard deviation of the last 1,000 data points and shown in Table 3. The table also presents the difference of maximum and minimum of the last 1,000 data points and the mean value.

Table 3. Estimation of random error based on statistical convergence of last 1,000 PIV data points for water and XG-100. The "Max-Min" column shows maximum minus minimum of the value.

	Water			XG-100		
	Mean	Standard deviation	Max-Min	Mean	Standard deviation	Max-Min
$u^2/ u_{\tau 0}^2$	4.23	0.0070	0.025	6.68	0.0098	0.0422
$v^2/ u_{\tau 0}^2$	0.53	0.0004	0.002	0.25	0.0004	0.0015
$uv/ u_{\tau 0}^2$	-0.61	0.0014	0.005	-0.37	0.0014	0.0058
$u^2v/ u_{\tau 0}^3$	0.75	0.0040	0.018	-0.10	0.0050	0.0222
$u^3/ u_{\tau 0}^3$	-3.76	0.0225	0.087	1.86	0.1930	0.637
$u^4/ u_{\tau 0}^4$	53.4	0.1016	0.365	108	0.3178	1.36

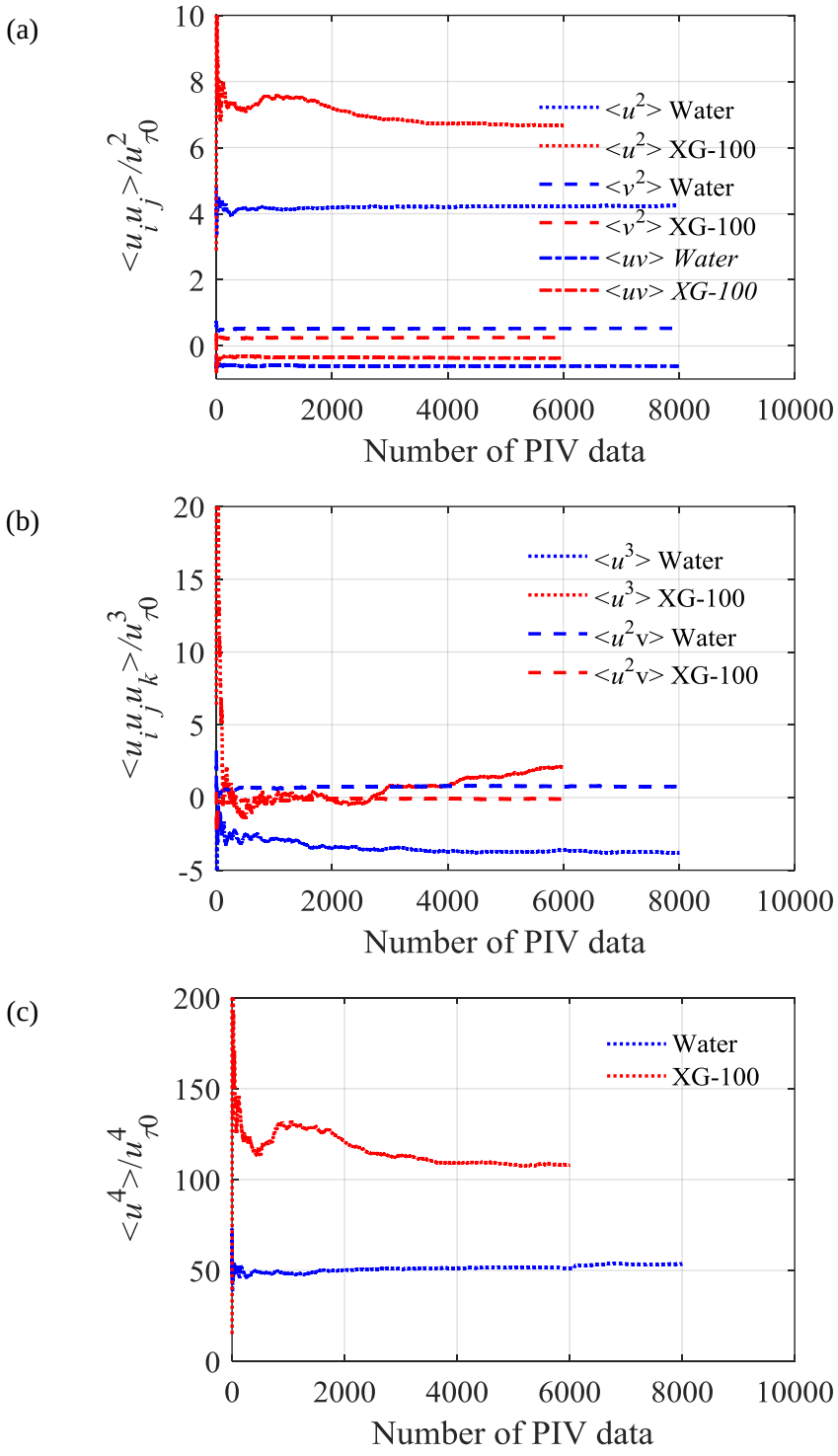

Figure 15. Statistical convergence of (a) $<u^2>/ u^2_{\tau 0}$,$<v^2>/ u^2_{\tau 0}$, and $<uv>/ u^2_{\tau 0}$, (b) $<u^3>/ u^3_{\tau 0}$, and $<u^2v>/ u^3_{\tau 0}$, and (c) $<u^4>/ u^4_{\tau 0}$ at y^+_0=25 for water and XG-100 versus number of PIV data points.

VI. References

[1] B.A. Toms, , "Some observations on the flow of linear polymer solutions through straight tubes at large Reynolds numbers," Proceedings of the 1st International Congress of Rheology, Vol. 2, Ed. J. M. Burgers. North Holland, Amsterdam, 135 (1949).

[2] T.S. Luchik, W.G. Tiederman, "Turbulent structure in low-concentration drag-reducing channel flows," J Fluid Mech 198, 241 (1988).

[3] M.D. Warholic, H. Massah, T.J. Hanratty, "Influence of drag-reducing polymers on turbulence: effects of Reynolds number, concentration and mixing," Experiment in Fluids 27, 461 (1999).

[4] A. Abubakar, T. Al-Wahaibi, Y. Al-Wahaibi, A.R. Al-Hashmi, A. Al-Ajmi, "Review, Roles of drag reducing polymers in single and multi-phase flows," chemical engineering research and design 92, 2153 (2014).

[5] H.A. Abdulbari, A. Shabirin, H.N. Abdurrahman, "Bio-polymers for improving liquid flow in pipelines-A review and future work opportunities," Journal of Industrial and Engineering Chemistry 20, 1157 (2014).

[6] B. Gampert, T. Braemer, T. Eich, T. Dietmann," Some experimental results on Laser Doppler Velocimetry (LDV) and birefringence (FIB) studies of non-newtonian fluids flow through rectangular channels,". 4th ASME_JSME Joint Fluids Engineering Conference (2003).

[7] B. Gampert, T. Braemer, T. Eich, T. Dietmann, "Rheo-optical investigations and near-wall turbulence structure of polymer solutions in turbulent channel flow," J. Non-Newt. Fluid Mech. 126, 115 (2005).

[8] M.P. Escudier, A.K. Nickson, R.J. Poole, "Turbulent flow of viscoelastic shear-thinning liquids through a rectangular duct: Quantification of turbulence anisotropy," Journal of Non-Newtonian Fluid Mechanics 160, 2 (2009).

[9] A. Jaafar, R.J. Poole, "Drag Reduction of Biopolymer Flows," Journal of Applied Sciences 11, 1544 (2011).

[10] A.S. Pereira, R.M. Andrade, E.J. Soares, "Drag reduction induced by flexible and rigid molecules in a turbulent flow into a rotating cylindrical double gap device: Comparison between Poly (ethylene oxide), Polyacrylamide, and Xanthan Gum," Journal of Non-Newtonian Fluid Mechanics 202, 72 (2013).

[11] C.A. Kim, , H.J. Choi, , C.B. Kim, , & M.S. Jhon,. "Drag reduction characteristics of polysaccharide xanthan gum." Macromolecular Rapid Communications 19, 419 (1998).

[12] H.-W. Bewersdorff, R.P. Singh, "Rheological and drag reduction characteristics of xanthan gum solutions," Rheologica Acta 27, 617 (1988).

[13] J.I. Sohn, C.A. Kim, H.J. Choi, , M.S. Jhon, , "Drag-reduction effectiveness of xanthan gum in a rotating disk apparatus," Carbohydrate Polymers 45, 61 (2001).

[14] J.L. Lumley, "Drag reduction by additives," Annu. Rev. Fluid Mech. 1(1), 367 (1969).

[15] P.G. De Gennes, “Towards a scaling theory of drag reduction,” Physica 140A, 9 (1986).

[16] C.M. White, and M.G. Mungal, ” Mechanics and prediction of turbulent drag reduction by polymer additives,” Annu. Rev. Fluid Mech. 40, 235 (2008).

[17] L. Thais, T.B. Gatski, and G. Mompean, “ Some dynamical features of the turbulent flow of a viscoelastic fluid for reduced drag,” Journal of Turbulence, Vol. 13, No.19, 1 (2012).

[18] K. Gasljevic, G. Aguilar, E.F. Matthys, “On two distinct types of drag-reducing fluids, diameter scaling, and turbulent profiles,” Journal of Non-Newtonian Fluid Mechanics 96, 405 (2001).

[19] P.S. Virk, “Drag reduction by collapsed and extended polyelectrolytes,” Nature 253, 109 (1975a).

[20] P.K. Ptasinski, F.T.M. Nieuwstadt, B.H.A.A. Van-Den, M.A. Hulsen, “Experiments in turbulent pipe flow with polymer additives at maximum drag reduction,” Turbulence Combustion 66, 159 (2001).

[21] Den Toonder, J.M.J., et al., “Degradation effects of dilute polymer solutions on turbulent drag rereduction in pipe flows,” Applied Scientific Research, 55(1): 63 (1995).

[22] N. Afzal, K. Yajnik, “Analysis of turbulent pipe and channel flows at moderately large Reynolds number,” J. Fluid Mech. 61, 23 (1973).

[23] B. Bhushan, “Biomimetics-Bioinspired Hierarchical-Structured Surfaces for Green Science and Technology,” (Springer Heidelberg New York Dordrecht London 2012) p.248.

[24] Y.A. Çengel, J.M. Cimbala,” Fluid mechanics : fundamentals and applications,” (3st ed.). New York: McGraw-Hill, p.353 (2014).

[25] M. Papagianni, S.K. Psomas, L. Batsilas, S. V. Paras, D. A. Kyriakidis, & M. Liakopoulou-Kyriakides, “Xanthan production by Xanthomonas campestris in batch cultures,” Process Biochemistry, 37, 73 (2001).

[26] K.D. Housiadas, & A.N. Beris, “Characteristic scales and drag reduction evaluation in turbulent channel flow of nonconstant viscosity viscoelastic fluids,” Physics of Fluids 16 (5), 1581 (2004)

[27] G. Schramm, “ A practical approach to rheology and rheometry (p. 121),” Karlsruhe: Haake (1994).

[28] P.S. Virk, Drag reduction fundamentals, American Institute of Chemical Engineers, 21, 625 (1975).

[29] C.D. Meinhart, S.T. Wereley, & J.G. Santiago, “A PIV Algorithm for Estimating Time-Averaged Velocity Fields,” Journal of Fluids Engineering, 122 (2), 285 (2000).

[30] M. Stanislas, L. Perret, and J. Foucaut, “Vortical structures in the turbulent boundary layer: A possible route to a universal representation,” J. Fluid Mech. 602, 327 (2008).

[31] P. Virk, H. Mickley, & K. Smith, “The ultimate asymptote and mean flow structure in Toms phenomenon,” Trans. ASME E: J. Appl. Mech 37, 488 (1970).

[32] T. Tsukahara, Y. Seki, H. Kawamura, and D. Tochio, "DNS of turbulent channel flow at very low Reynolds numbers," In Proc. of the Forth Int. Symp. on Turbulence and Shear Flow Phenomena, Williamsburg, USA, pp. 935 (2005).
[33] I. Procaccia and V.S. L'vov, "Colloquium: Theory of drag reduction by polymers in wall-bounded turbulence," Reviews of Modern Physics, 80, 225 (2008).

[34] T. Wei, and W. W. Willmarth, "Modifying turbulent structure with drag-reducing polymer additives in turbulent channel flows," J. Fluid Mech 245, 619 (1992).

[35] M.D. Warholic, D.K. Heist, M. Katcher, T.J. Hanratty, "A study with particle-image velocimetry of the influence of drag-reducing polymers on the structure of turbulence," Experiment in Fluids 31, 474 (2001).

[36] K. Iwamoto, Y. Suzuki, N. Kasagi, "Reynolds number effect on wall turbulence: toward effective feedback control," International Journal of Heat and Fluid Flow 23, 678 (2002).

[37] R., Theunissen, F., Scarano, M. L. Riethmuller, "On improvement of PIV image interrogation near stationary interfaces," Experiments in Fluids, 45(4), 557 (2008).

[38] J.M. Wallace, H. Eckelmann, and R.S. Brodkey, "The wall region in turbulent shear flow," J. Fluid Mech 54, 39 (1972).

[39] J. Kim, P. Moin, and R. Moser, "Turbulence statistics in fully developed channel flow at low Reynolds number," J. Fluid Mech 177, 133 (1987).

[40] D. T. Walker, and W. G. Tiederman, "Turbulent structure in a channel flow with polymer injection at the wall," J. Fluid Mech 218, 377 (1990).

[41] Z. Fu, T. Otsuki, M. Motozawa, T. Kurosawa , B. Yu , Y. Kawaguchi, "Experimental investigation of polymer diffusion in the drag-reduced turbulent channel flow of inhomogeneous solution," International Journal of Heat and Mass Transfer 77, 860 (2014).

[42] K. Kim, A.I. Sirviente, "Turbulence structure of polymer turbulent channel flow with and without macromolecular polymer structures," Experiment in Fluids 38, 739 (2005).

[43] C.M. White, V.S.R. Somandepalli, M.G. Mungal, "The turbulence structure of drag-reduced boundary layer flow," Experiment in Fluids 36, 62 (2004).

[44] L. Sirovich,"Turbulence and the Dynamics of Coherent Structures. Part 1: Coherent Structures," Quarterly of Applied Mathematics 45(3), 561 (1987).

[45] J.L. Lumley, "The structure of inhomogeneous turbulent flow," In Atmospheric Turbulence and Radio Wave Propagation (ed. A. M. Yaglom & V. I. Tatarski), Nauka, Moscow 166 (1967).

[46] K. Meyer, J. Pedersen, and O. Ozcan,"A turbulent jet in crossflow analysed with Proper Orthogonal Decomposition," J. Fluid Mech., 583, 199 (2007).

[47] K. Robinson, "Coherent motions in the turbulent boundary layer," Annu. Rev. Fluid Mech. 23, 601 1991.

[48] A. V. Johansson, P. H. Alfredsson, H. Eckelmann, "Advances in Turbulence," (Springer-Verlag Berlin Heidelberg 1987) P.384.

[49] H. Kreplin, H. Eckelmann, "Propagation of perturbations in the viscous sublayer and adjacent wall region," J. Fluid Mech., 95(2), 305 (1979).

[50] W.-H. Cai, F.-C. Li, H.-N. Zhang, X.-B. Li, B. Yu, J.-J. Wei, Y. Kawaguchi, and K. Hishida, "Study on the characteristics of turbulent drag-reducing channel flow by particle image velocimetry combining with proper orthogonal decomposition analysis," Physics of Fluids 21, 115103 (2009).